Check for updates

Received: 6 March 2020 | Revised: 31 January 2021 | Accepted: 3 February 2021

DOI: 10.1111/rge.12262

ORIGINAL ARTICLE

RESOURCE GEOLOGY WILEY

The Hera orebody: A complex distal (Au–Zn–Pb–Ag–Cu) skarn in the Cobar Basin of central New South Wales, Australia

Joel A. Fitzherbert[1] | **Adam R. McKinnon**[2] | **Phillip L. Blevin**[1] | **Kathryn Waltenberg**[3] | **Peter M. Downes**[1] | **Corey Wall**[4] | **Erin Matchan**[5] | **Huiqing Huang**[6]

[1]Geological Survey of New South Wales, Maitland, New South Wales, Australia

[2]Aurelia Metals Limited, Brisbane, Queensland, Australia

[3]Geoscience Australia, Symonston, Australian Capital Territory, Australia

[4]Department of Geosciences, Boise State University, Boise, Idaho

[5]School of Earth Sciences, University of Melbourne, Melbourne, Victoria, Australia

[6]Geoscience Division of Tropical Environments & Societies James Cook University, Townsville, Queensland, Australia

Correspondence
Joel A. Fitzherbert, Geological Survey of New South Wales, Maitland, NSW 2320.
Email: joel.fitzherbert@industry.nsw.gov.au

Abstract

The Hera Au–Pb–Zn–Ag deposit in the southeastern Cobar Basin of central New South Wales preserves calc-silicate veins and remnant sandstone/carbonate-hosted skarn within a reduced anchizonal Siluro-Devonian turbidite sequence. The skarn orebody distribution is controlled by a long-lived, basin margin fault system, that has intersected a sedimentary horizon dominated by siliciclastic turbidite, with lesser gritstone and thick sandstone intervals, and rare carbonate-bearing stratigraphy. Foliation (S1) envelopes the orebody and is crosscut by a series of late-stage east–west and north–south trending faults. Skarn at Hera displays mineralogical zonation along strike, from southern spessartine–grossular–biotite–actinolite-rich associations, to central diopside-rich–zoisite–actinolite/tremolite–grossular-bearing associations, through to the northern most tremolite–anorthite-rich (garnet-absent) association in remnant carbonate-bearing lithologies and sandstone horizons; the northern lodes also display zonation down dip to garnet present associations. High-T, prograde skarn assemblages rich in pyroxene and garnet are pervasively replaced by actinolite/tremolite–biotite-rich retrograde skarn which coincides with the main pulse of sulfide mineralization. The dominant sulfides are high-Fe–Mn sphalerite–galena–non-magnetic high-Fe pyrrhotite–chalcopyrite; pyrite, arsenopyrite; scheelite (low Mo) is locally abundant. The distribution of metals in part mimics the changing gangue mineralogy, with Au concentrated in the southern and lower northern lode systems and broadly inverse concentrations for Ag–Pb–Zn. Stable isotope data (O–H–S) from skarn amphiboles and associated sulfides are consistent with magmatic (or metamorphic) water and sulfur input during the retrograde skarn phase, while hydrosilicates and sulfides from the wall rocks display comparatively elevated δD and mixed $\delta^{34}S$ consistent with progressive mixing or dilution of original magmatic (or metamorphic) waters within the Hera deposit by unexchanged waters typical of low latitude (tropical) meteoritic waters. High precision titanite

This is an open access article under the terms of the Creative Commons Attribution License, which permits use, distribution and reproduction in any medium, provided the original work is properly cited.
© 2021 The Authors. *Resource Geology* published by John Wiley & Sons Australia, Ltd on behalf of Society of Resource Geology

(U–Pb) and biotite (Ar–Ar) geochronology reveals a manifold orebody commencing with high-T skarn and retrograde Pb–Zn-rich skarn formation at ≥403 Ma, Au–low-Fe sphalerite mineralization at 403.4 ± 1.1 Ma, foliation development remobilization or new mineralization at 390 ± 0.2 Ma followed by thrusting, orebody dismemberment at 384.8 ± 1.1 Ma and remobilization or new mineralization at 381.0 ± 2.2 Ma. The polymetallic nature of the Hera orebody is a result of multiple mineralization events during extension and compression and involving both magmatic and likely formational metal sources.

KEYWORDS

Ar–Ar geochronology, Cobar Basin, mineral chemistry, skarn, stable isotopes, U–Pb geochronology

1 | INTRODUCTION

The Siluro-Devonian Cobar Basin is a major mining province in central New South Wales, Australia. The area hosts small to large polymetallic precious and base-metal deposits including those in the Cobar mineral field (Endeavor, CSA, New Cobar, Chesney, New Occidental, Peak and Perseverance mines) as well as the Hera mine and Nymagee deposit to the southeast. Past production and identified resources for the Cobar Basin exceeds 134.9 t Au, 1.91 Mt Cu, 3.46 Mt Zn, 1.8 Mt Pb and 3,832 t Ag (to the end 2015; Seccombe *et al*., 2017).

Orebodies of the Cobar Basin have been variously classified through time as reactivated/remobilized syn-depositional sub-exhalative to exhalative deposits (Suppel, 1984), epithermal and volcanogenic massive sulfide deposits (David, 2005, 2006), but more recently an orogenic sulfide–Au model has been applied, with mineralizing fluids derived from a mixing of basement and basinal fluids during burial (e.g., Lawrie and Hinman, 1998; Stegman, 2001; Seccombe *et al*., 2017).

Cobar Basin orebodies share many unifying features including:

- Intimate relationship with major, long-lived basin forming fault systems;
- Lithological control, either through permeability (sandstone-hosted orebodies), reactivity (carbonates and feldspathic igneous rocks; sandstone), competency contrast (between rhyolite/porphyry, sandstone and fine-grained sedimentary rocks); and,
- Orebody morphology is similar, with many orebodies comprising a series of carrot-like, steep-dipping, short strike length lenses with a large vertical extent. Many ore zones are polymetallic, often with spatially separated Pb–Zn–Ag, Cu–Au and even Zn–Au lenses.

These unifying features provide a framework for understanding how ore-bearing fluids were transported and potential trapping mechanisms, but a lack of well-constrained, direct age dating of mineralization events leaves the energy, fluid and metal sources for mineralization ambiguous. Isotopic studies have been used to suggest the sulfur and metal reservoirs (e.g., Lawrie and Hinman, 1998; Stegman, 2007; Seccombe *et al*., 2017; Downes and Poulson, 2018). Isotopic characteristics can provide a piece to the puzzle but do not give a unique solution, particularly in the absence of well constrained temporal and spatial discrimination of the results.

Limited work has been conducted on the early phase of mineralization for the orebodies in the main Cobar mining district due to the intense overprinting deformation fabrics, ore remobilization and overprinting phases of mineralization. Below we present a detailed petrographic, isotopic and geochronological study of the polymetallic Hera orebody in the southeastern Cobar Basin. Our data strengthens an intrusion-related, skarn genesis for the early phase of mineralization at Hera, as suggested by Fitzherbert *et al*. (2017a, b), and highlights the longevity and manifold nature of mineralization required to assemble a complex polymetallic Cobar Basin orebody.

2 | GEOLOGICAL SETTING

The Cobar Basin is an extensional basin that was deposited over basement of Ordovician turbidite and S-type Silurian granites during the late Silurian to Early Devonian (Figure 1). Deep-water parts of the basin interfinger with two volcanogenic troughs, to the south (Rast Group) and west (Mount Hope Group) and are flanked by limestone-bearing shelf sequences to the west (Winduck Group), as well as limestone and shallow water to subaerial syn-rift volcanic sequences in the east (Kopyje Group)

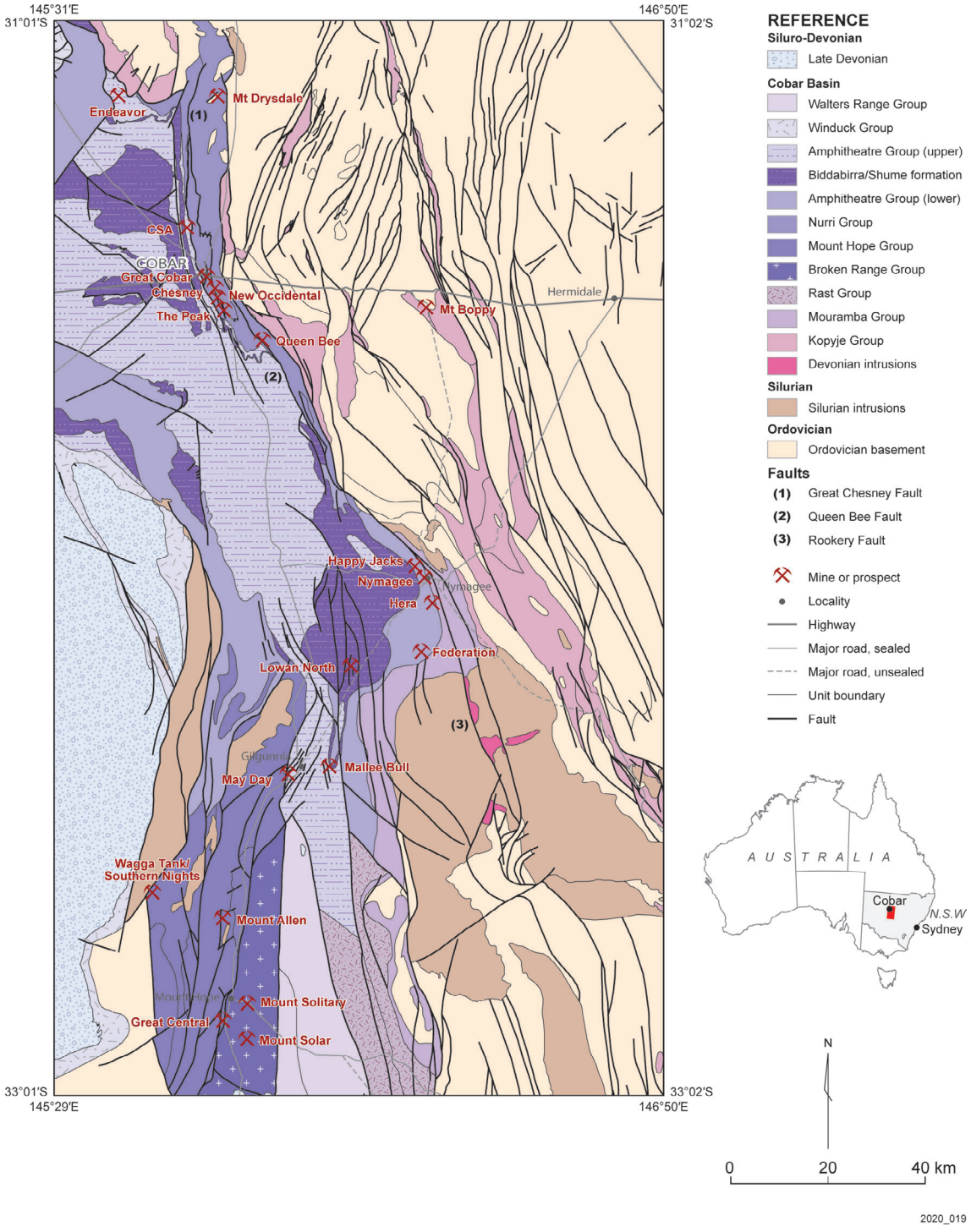

FIGURE 1 Group-level distribution of the Cobar Supergroup and underlying basement. Undercover interpretation is based on Fitzherbert *et al.* (2017a, b)

(Figure 1). The lower stratigraphic levels of the southeastern deep-water basin, shelf sequences and Ordovician basement sequences are intruded by syn-rift Early Devonian I-type plutons along the eastern margin of the basin and adjacent shelf sequences (Figure 1). The Cobar Basin is thought to have been inverted and deformed over 25 million years between 405 to 380 Ma (Perkins *et al.*, 1994; Glen *et al.*, 1996). Basin inversion was associated with reactivation of major basin/trough margin faults or near margin faults. Most Cobar Basin-hosted orebodies are concentrated in a belt along the eastern margin of the deep-water Basin (Figure 1). These deposits are mostly associated with zones of faulting, shear zone development and epizone hydrothermal alteration, although the

effects of deformation are relatively diminished to the south and hydrothermal metamorphic grades are significantly higher (hornblende hornfels facies).

Mineralization in the main (northern) Cobar mineral field is associated with greenschist facies high-strain zones and is linked with fluids that exploited major fault systems and regional lithological contacts. Correlative mineralization along these same fault systems and lithological contacts occurs on the southeastern margin of the basin, hosted within siliciclastic-dominant turbidite sequences of the lower Amphitheater Group and to a lesser extent shallow-water carbonate-bearing sequences of the Mouramba Group (Figure 1). The deposits are spatially associated with a major basin margin fault, the Rookery Fault, although the major orebodies are located immediately west of this fault system.

The genetic process(es) that have driven mineralization in the Cobar Basin remain unclear. Rifting and deposition of the mineralized sequences occurred after ca. 424 Ma (youngest age of exhumed basement rocks; Downes *et al*., 2016), but synchronous with intrabasin volcanism dated at 420–417 Ma (Downes *et al*., 2016); The youngest identified syn-rift intrusions/volcanics within, and immediately adjacent to the Cobar Basin are c. 411 Ma (Jones *et al*., 2020), although the upper parts of the volcanogenic Rast Trough, to the south, are dated at c. 412 Ma (Downes *et al*., 2016) and c. 409 Ma (Bull *et al*., 2008), signifying that rift-related volcanism extended into the Pragian (410.8 ± 2.8 to 407.6 ± 2.6 Ma—time scale of Gradstein *et al*. 2012). The youngest preserved basin fill is thought to be lowest Emsian c. 405 Ma (van der Wielen and Glen, 2008; Glen *et al*., 2016), potentially even Emsian (c. 400 Ma; Parrish *et al*., 2018) (Emsian, 407.6 ± 2.6 to 393.3 ± 1.2 Ma—time scale of Gradstein *et al*. 2012). Shallow-water sequences on the faulted eastern and western flanks of the Cobar Basin host Pragian to earliest Emsian limestone (*sulcatus* (lower Pragian) to *dehiscenz* (lowest Emsian) conodont zones (c. 406 Ma; Mathieson *et al*., 2016).

Inversion of the basin during the Tabberabberan Orogeny is thought to have been initiated c. 400 Ma (Glen *et al*., 1992), with continued compression until c. 380 Ma (Downes *et al*., 2016); a similar 20 million year interval for the Tabberabberan Orogeny is observed throughout south-eastern Australia (Fergusson, 2017). Fitzherbert *et al*. (2017a, b) demonstrated that sedimentary packages of the Cobar Basin did not undergo deep burial during this inversion and perceived biotite-zone greenschist facies and above regional metamorphic grades are related to, pre-foliation, hydrothermal highs associated with zones of mineralization. In fact, many Cobar Basin orebodies show evidence for mineralization and peak (highest temperature) hydrothermal alteration pre- or potentially early syn-foliation development, suggesting the initial mineralization event is ≥400 Ma. This does not preclude subsequent pulses of mineralization during periods of movement on large basinal faults with or without associated magmatism. Syn- to late-orogenic Pb–Zn–(Ag) mineralization has been recorded for several orebodies in the Cobar Basin, including the Endeavor, Manuka and even CSA. It is also well documented that the adjacent Cu–Au mineralization is significantly older (e.g., Lawrie and Hinman, 1998).

3 | DEPOSIT DESCRIPTION

The Hera orebody is an Au–Pb–Zn–Ag-rich orebody with a mineral resource (combined measured, indicated, inferred) totaling 2061 kt at 1.8 g/t Au, 2.8% Pb, 4.2% Zn and 34 g/t Ag (Aurelia Metals Ltd 2019 Annual Report to the Australian Stock Exchange, 30th October 2019 https://www.aureliametals.com/investors/annual-reports).

3.1 | Geometry

The Hera orebody is interpreted as a single fault-controlled, but grossly stratabound massive sulfide breccia body (McKinnon and Fitzherbert, 2017) with a general strike of 330°, dip of ~80° west and an overall plunge of 020° north at its base. A single satellite lens (Kershaws lode) occurs east of the main orebody. The orebody has been cut by a series of late-stage north-oriented faults striking between 005–015° and dipping 75° east, as well as by lesser east–west faults striking 110° and dipping 80° south. These late faults result in a series of steeply-dipping (80° west), west-stepping ore lodes that strike 337–344°, with apparent short strike lengths, apparent steep plunges and large vertical extent (Figure 2).

3.2 | Metal distribution

Hera has elevated Au, Ag, Cu, Pb and Zn. In terms of metal distribution and major sulfides, Au is relatively widespread at Hera, but there is a clear negative correlation between Au and Ag abundance with Ag elevated only in the upper North Pod and upper Far West lode (Figure 3). Galena and sphalerite are uniformly abundant. There is a negative correlation observed between Pb–Zn and Au abundance, and a positive correlation between Pb–Zn and Ag abundance (Figure 3). There is also a positive correlation between Ag–Pb–Zn abundance and the abundance of carbonate-hosted skarn, while Au has the inverse relationship (Figure 3).

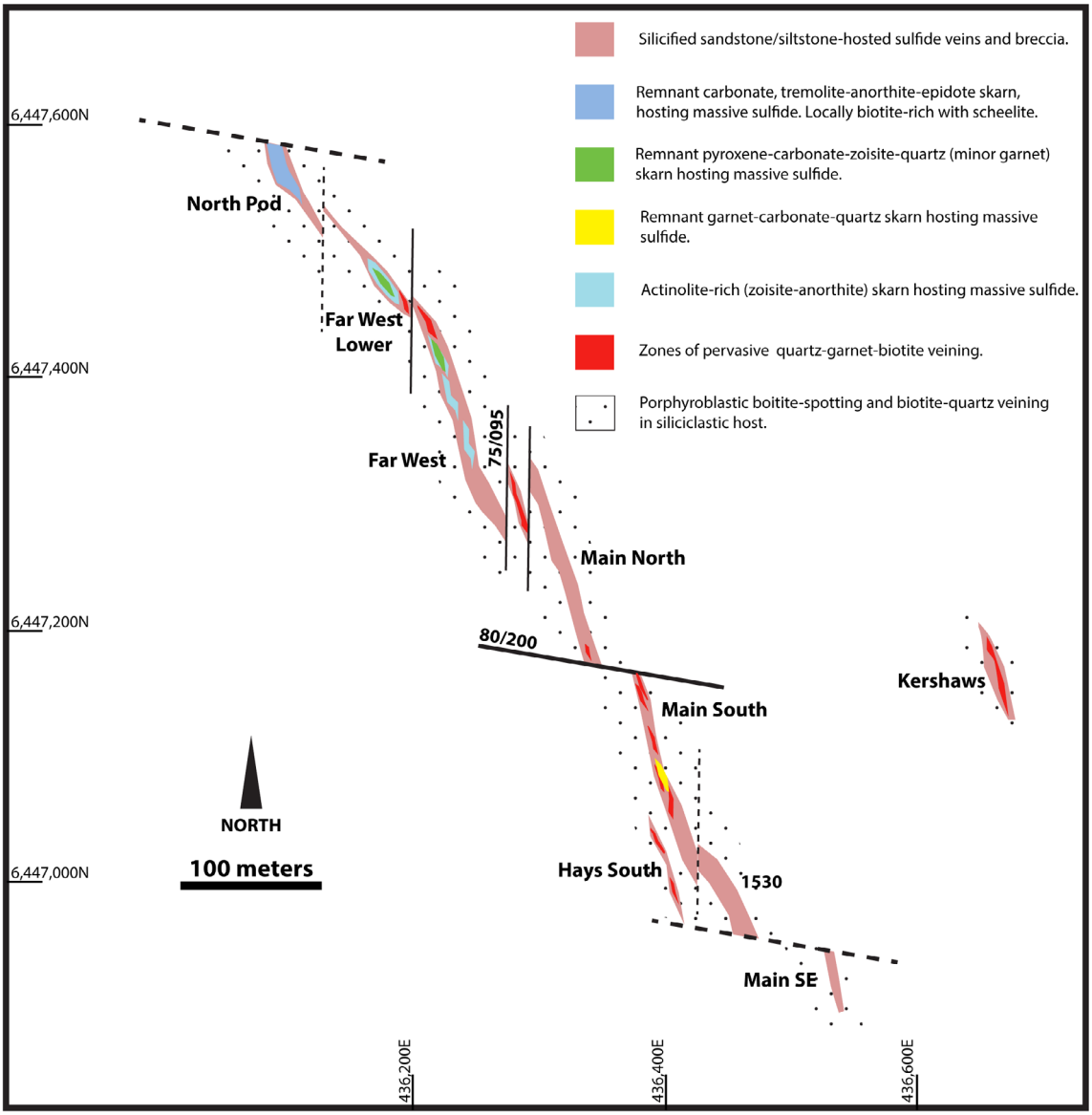

FIGURE 2 Surface projected plan view of the Hera orebody depicting the various fault-bound lodes. The orebody is solely hosted in the lower Amphitheater Group

Pyrrhotite and pyrite are concentrated in the upper parts of all lodes. Pyrrhotite is ubiquitous within the North Pod while pyrite is low in abundance except at the top of the Main South and Main North lodes (Figure 3). In addition, arsenopyrite is abundant in the North Pod while chalcopyrite is widespread toward the upper parts of most lodes and reports to a similar location as Fe-sulfides. The general sulfide paragenesis is presented in Figure 4 and is discussed further below.

3.3 | Host rocks

The Hera orebody is hosted in the deep-water lower Amphitheatre Group of the Cobar Supergroup. The local geology around the mine sequences is dominated by thin bedded to laminated, fine-grained sandstone and siltstone. This fine-grained sedimentary facies is rich in quartz and albite, with abundant detrital white mica, biotite and Fe–Ti oxides. McKinnon and Fitzherbert (2017) described the destruction of host rock feldspar and detrital biotite (using hole rock chemistry and hyperspectral data) as far as 135 m away from the Hera orebody; detrital Fe–Ti oxides are also replaced by hydrothermal titanite over a similar distance from the orebody. Thick-bedded sandstone and gritstone intervals are prominent within the mineralized interval and although mineralogically similar to the fine-grained equivalents, much of the skarn alteration is focused in and around these beds. In addition, McKinnon and Fitzherbert (2017) described a

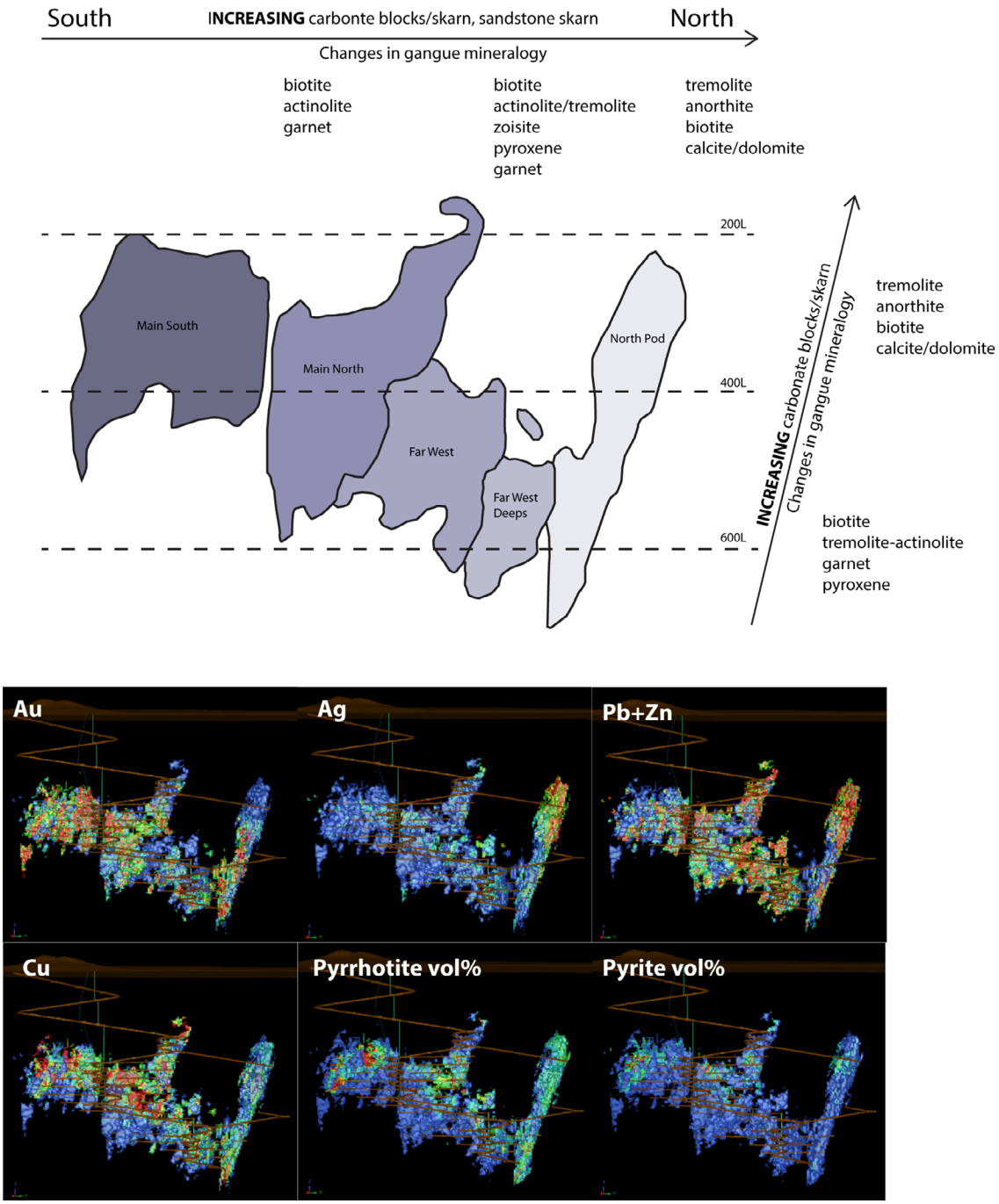

FIGURE 3 Long section of the Hera orebody looking west including metal distribution and general changes in gangue mineralogy. Pyrrhotite and pyrite vol% calculated according to McKinnon (2017)

northerly increase in dolomitic zones within the orebody, with rare laminated dolomite clasts preserved within zones of massive sulfide within the North Pod.

3.4 | Skarn and alteration mineralogy

Mineralization occurs in vein/breccia zones predominantly hosted by intensely silicified, siliciclastic sequences (siltstone, sandstone and gritstone). A halo of porphyroblastic hydrothermal biotite surrounds the orebody. This halo extends for 10s of meters into the host siliciclastic sedimentary rocks. The deposits high-T, prograde skarn mineralogy has two main textural forms, siliciclastic-hosted veins and breccia fill (siliciclastic-hosted skarn) hosted mainly within siltstone-rich sequences, and sandstone/carbonate replacement skarn (sandstone/carbonate skarn) hosted mostly within

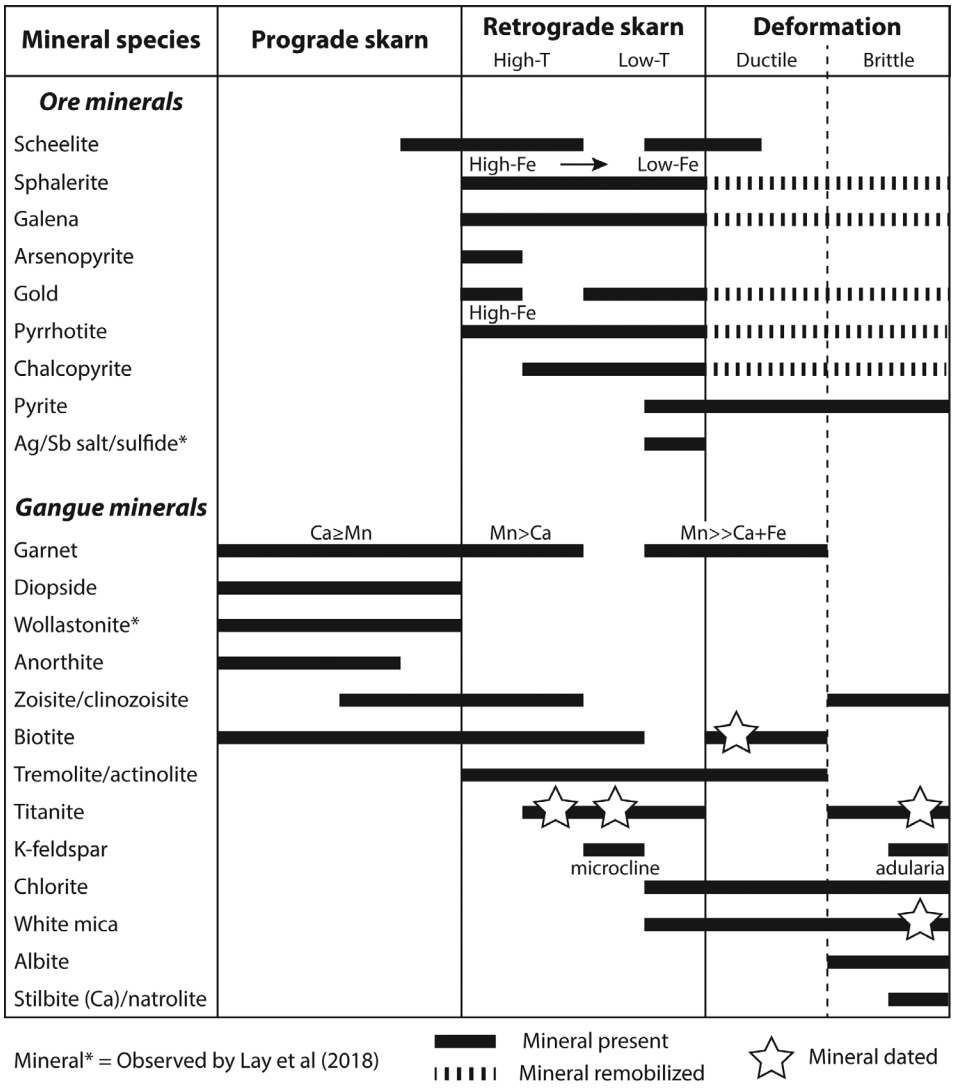

FIGURE 4 Combined ore and gangue mineral paragenesis for the Hera orebody

sandstone, gritstone with rare carbonate (dolomitic) clasts. Prograde skarn is overprinted by two main pulses of retrograde alteration; a sulfide-rich phase with moderate-T hydrous-mineral-rich retrograde skarn and late-stage of low-T hydrous mineral-rich hydrothermal alteration. Figure 4 shows the general ore and gangue mineral paragenesis for the Hera orebody, while Figure 5 illustrates the spatial distribution of the main paragenetic phases and common crosscutting relationships.

Siliciclastic-hosted calc-silicate veins and breccia fill are, by far, the most commonly preserved form of high-T prograde skarn. In general, siliciclastic horizons and clasts are intensely silicified and enveloped by sulfide-rich breccias/veins. These frequently contain quartz-rich veins with garnet–zoisite–titanite–tremolite ± scheelite (low Mo) proximal to and within the sulfide orebody (Figure 6a). A biotite-rich mineralogy is also present distal to the orebody. Garnet within these veins displays strong chemical zonation (described below) from grossular-rich cores with calcite inclusions to spessartine-rich rims, which coincide with actinolite–zoisite and massive sulfide mineralization (Figure 6b). Veins are commonly enveloped by a 10–200 mm wide zoned alteration halo. This typically includes fine-grained garnet–titanite–anorthite–zoisite proximal to veins, then garnet–actinolite–anorthite–zoisite, followed by actinolite–biotite–anorthite and finally distal biotite–muscovite-rich zones that meld with the porphyroblastic biotite alteration halo surrounding the deposit. Garnet is absent from siliciclastic skarn in the North Pod.

Remnant zones of High-T, prograde skarn occur within and adjacent to the mineralized sequence and may occur as pods, as a replacement after sandstone horizons and/or after carbonate clasts/blocks (Figure 5). These comprise a grossular–quartz–diopside–actinolite–zoisite–anorthite ± carbonate (often dolomitic) assemblage (Figures 6c,d). The remnant high-T, prograde skarn zones display a broad mineralogical zonation along the entire strike of the orebody from a garnet-rich in the southern lenses, to

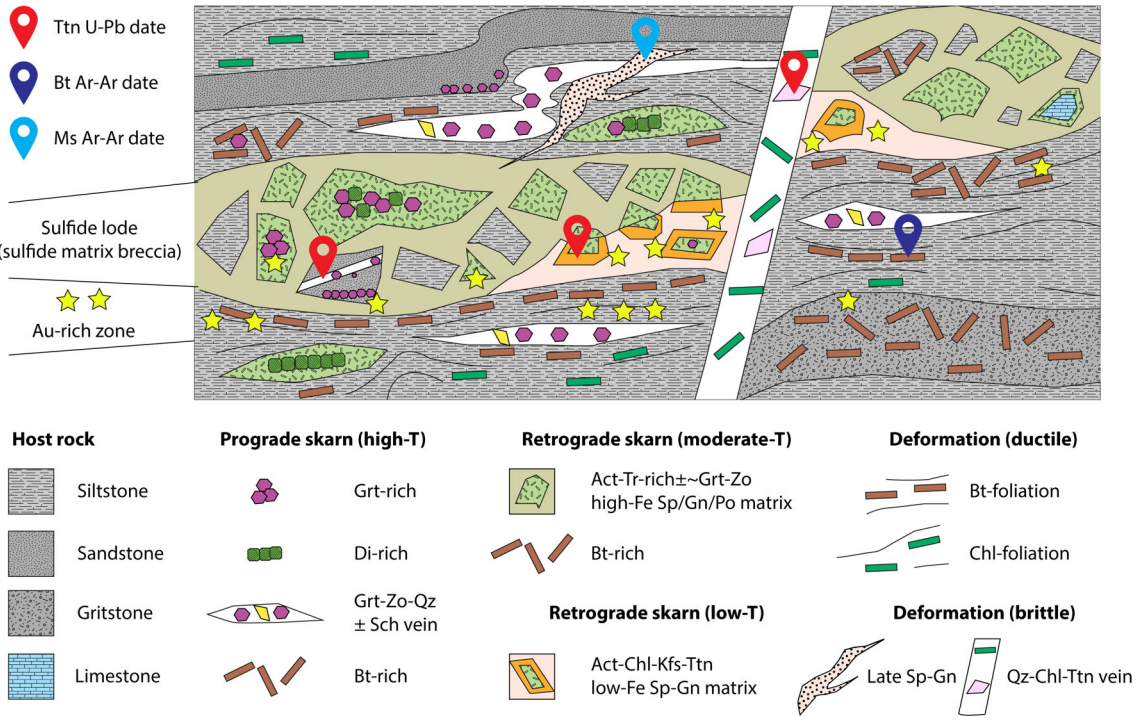

FIGURE 5 Idealized rock relationships diagram depicting potential overprinting paragenesis in a single ore lens (plan view). Mineral abbreviations according to Whitney and Evans (2010)

pyroxene-rich assemblage in the Far West lenses (Figure 6e), and tremolite–biotite–anorthite ± (scheelite) assemblage (Figure 6f) in the upper North Pod while there is a garnet-bearing assemblage in the lower North Pod.

The retrograde skarn phase is ubiquitous, enveloping prograde skarn throughout the orebody. This hydrous retrograde skarn is sulfide-rich and shows a progression from moderate-T to low-T mineral associations. Moderate-T retrograde skarn is the dominant expression of this phase, often with a high-Fe sphalerite–galena–pyrrhotite ± chalcopyrite assemblage (Figures 4, 5, and 6g). Pyrite is locally abundant, particularly toward the upper margins of ore lenses with the gangue dominated by actinolite–tremolite–biotite±spessartine. Although in many parts of the North Pod this hydrous phase consists of monomineralic tremolite in addition to abundant sulfides. The sulfide mineralogy of North Pod is also more variable. Arsenopyrite is locally more abundant, in addition to the other sulfides, and there are silver sulfosalts and elemental silver in upper North Pod. Gold is often, but not exclusively associated with sulfides. It occurs in association with moderate-T retrograde skarn, but also occurs within the sandstone and siltstone external to the main sulfide zone, often remobilized within the main foliation.

A distinctive low-Fe orange colored sphalerite (Figure 6h,i) is often associated with nuggety-gold and occurs as infill between breccia clasts of the hydrous retrograde skarn. Very localized K-feldspar–titanite-rich assemblages are developed in the altered host rock selvage to low-Fe sphalerite mineralization and appear to postdate the moderate-T retrograde skarn (Figure 6i).

The final stage of skarn-related alteration involves variable development of late-stage low-T, hydrous chlorite–muscovite-rich ± rare almandine assemblages, often associated with galena and low-Fe sphalerite.

The Hera orebody is enveloped by variably developed foliation with a biotite–tremolite–white mica–talc assemblage. Sulfide-rich stringers often parallel the foliation and may reflect a new phase of mineralization or, more likely, zones of remobilized ore (Figure 6j). Native gold can also be present in the biotite-rich foliation that envelopes the orebody. Biotite and tremolite within the foliation are variably retrogressed to chlorite-rich associations late in the ductile phase of deformation.

The orebody and overprinting foliation are cut by late-stage, west-verging reverse faults defined by quartz-rich veins with titanite, clinozoisite, chlorite, albite, adularia, tourmaline and zeolite (Figures 5 and 6k). These are generally barren but minor high-Fe sphalerite can be present, although a single fibrous tourmaline-rich vein was observed to contain abundant native gold. These

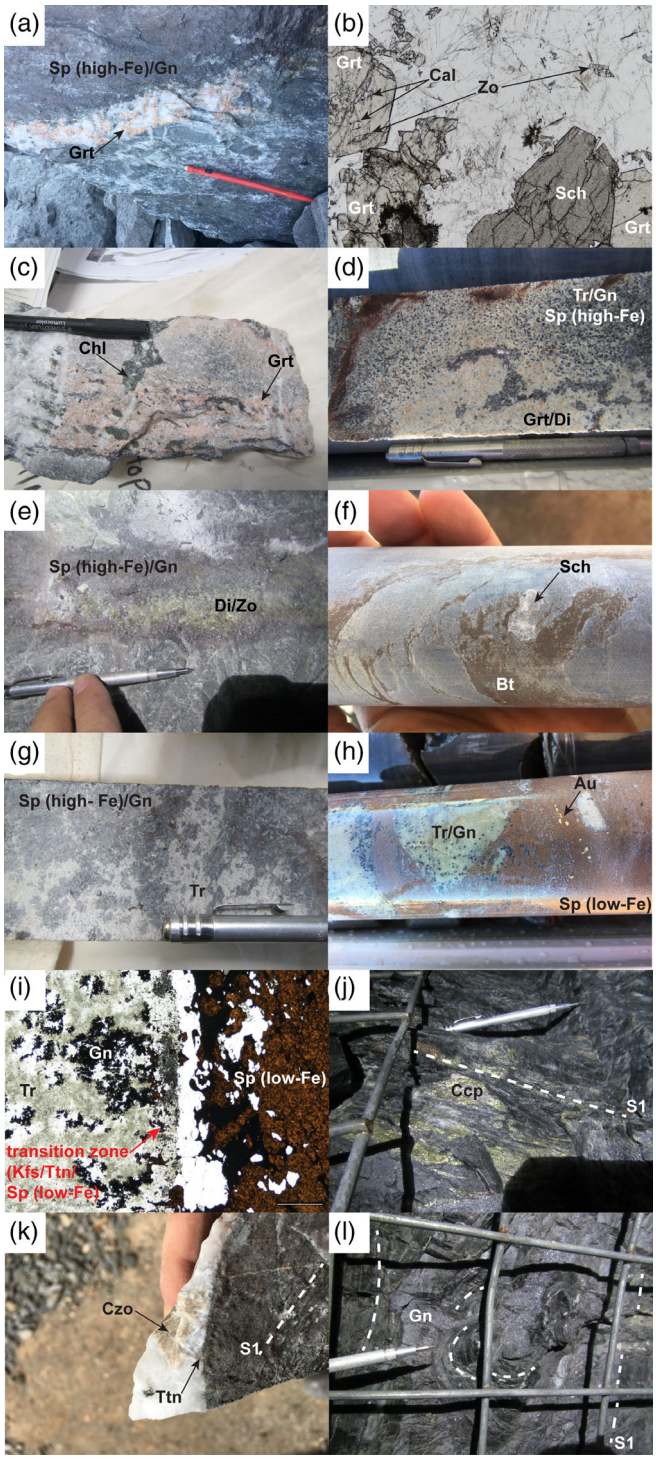

FIGURE 6 (a) Garnet–quartz veins from siliciclastic skarn. Note the high-Fe sphalerite and galena above the vein. Sample from the Main North lode. (b) Photomicrograph of quartz–garnet–scheelite–zoisite vein. The inclusions in the core of garnet (red arrow) are calcite, while zoisite is the only inclusion phase to garnet rims and within the veins. (c) Silicified and garnet-flooded sandstone horizon. Note the late-stage quartz–chlorite-rich veins associated with partial replacement of skarn garnet. (d) Remnant garnet–diopside skarn block likely developed in a sandstone unit. Note the replacement (mostly of diopside) by retrograde tremolite and sulfide skarn around the margins of the high-T skarn fragment. Far West lode. (e) Pod of diopside-rich skarn from the Far West lode. Note the strong sulfide replacement around the margins. (f) Irregular biotite–scheelite veins within a siliclastic host from the North Pod. (g) Typical retrograde, sphalerite–galena–tremolite skarn. (h) Low-Fe sphalerite and gold forming the matrix to a brecciated tremolite-enriched hydrous skarn. The black spots are radiating clusters of galena that are typically seen replacing pyroxene within the hydrous skarn. Far West lode. (i) Margin of the low Fe-sphalerite–gold vein. Left is retrograde tremolite–galena skarn, right is high Fe-sphalerite–quartz–gold breccia matrix. The thin transition zone between the two is marked by replacement of the hydrous skarn by quartz–K-feldspar–low Fe-sphalerite–titanite. Far West lode. (j) Chalcopyrite within the biotite-rich S1 foliation (red dashed line) that envelopes the orebody. The foliation is well developed in the biotite-rich selvage around the orebody. Far West lode. (k) Late-stage quartz–clinozoisite (buff colored) titanite veins cross-cutting the S1 foliation that envelopes the orebody (red dashed line). (l) Massive galena mineralization cross cutting folded S1 foliation that envelopes the orebody (red dashed lines)

veins are predominantly chlorite-rich throughout the orebody but abruptly switch to being biotite-rich in the Far West Deeps and lower North Pod (below 535 level) zones.

Sulfide-rich zones that cross-cut foliation are commonly observed (Figure 6l). These may be a minor late mineralization stage or be zones of remobilized ore.

4 | RESULTS

4.1 | Mineral chemistry

Microprobe analyses for garnet, amphibole, epidote, feldspar, pyroxene, biotite and chlorite were collected with a Cameca SX–100 Camebax microprobe at the Australian National University. Results are discussed below. Representative data are presented in Table 1.

Garnet is compositionally variable depending on textural location and may be complexly zoned. The andradite content of garnet is minimal with analyses normalizing to three components: Xgrs (grossular) = Ca/(Fe + Mn + Mg + Ca), Xsps (spessartine) = Mn/(Fe + Mn + Mg + Ca) and Xalm (almandine) = Fe^{2+}/(Fe^{2+} + Mn + Mg + Ca). Garnet composition varies according to its spatial setting and timing (Figure 7a).

Garnet within prograde skarn associations, siliciclastic vein/breccia (quartz–low Mo scheelite–zoisite-rich; Figure 6a,b) and/or sandstone/carbonate replacement (garnet–pyroxene-rich skarn; Figure 6d,e) have an elevated grossular component compared to

TABLE 1 Representative microprobe data represented as weight percent oxide and recalculated cation proportions

	Garnet		Garnet		Garnet			Garnet			Garnet	
	External to Main lode		External to Main lode		Within Main lode			Within Main lode			Unretrogressed skarn	
	Core	Rim	Core	Rim	Core	Shoulder	Rim	Rim	Shoulder	Rim	Core	Rim
SiO_2	38.56	38.05	38.07	37.40	37.47	38.33	37.45	37.05	38.91	38.22	39.38	38.68
TiO_2	0.38	0.33	0.36	0.19	0.08	0.30	0.17	0.25	0.29	0.15	0.32	0.26
Al_2O_3	21.64	21.64	21.65	21.83	21.42	20.62	21.88	21.40	20.79	21.35	21.36	21.28
Cr_2O_3	0.00	0.00	0.00	0.00	0.01	−0.01	0.01	0.00	0.00	0.00	−0.01	−0.01
FeO	4.86	5.94	6.11	10.92	6.06	6.77	11.31	5.45	6.58	11.00	7.99	7.88
MnO	11.02	17.60	11.63	18.08	22.01	18.54	19.98	23.09	18.51	19.54	10.68	10.71
MgO	0.07	0.18	0.05	0.43	0.23	0.69	0.53	0.17	0.72	0.46	0.07	0.08
CaO	24.02	16.91	22.59	11.75	12.99	15.14	9.63	12.52	15.28	10.08	20.55	20.89
Na_2O	0.00	0.00	0.00	0.00	0.00	0.00	0.00	0.00	0.01	−0.01	0.01	0.00
K_2O	−0.01	0.00	0.00	0.00	0.01	0.01	0.00	0.00	0.00	0.01	0.00	0.01
Total	100.56	100.65	100.47	100.61	100.29	100.39	100.96	99.93	101.09	100.81	100.35	99.79
Num ox	24.00	24.00	24.00	24.00	24.00	24.00	24.00	24.00	24.00	24.00	24.00	24.00
Si	5.96	5.96	5.91	5.93	5.95	6.04	5.94	5.91	6.09	6.07	6.14	6.06
Ti	0.04	0.04	0.04	0.02	0.01	0.04	0.02	0.03	0.03	0.02	0.04	0.03
Al	3.94	4.00	3.96	4.08	4.01	3.83	4.09	4.03	3.83	4.00	3.92	3.93
Cr	0.00	0.00	0.00	0.00	0.00	0.00	0.00	0.00	0.00	0.00	0.00	0.00
Fe^{2+}	0.57	0.78	0.65	1.44	0.73	0.88	1.50	0.64	0.86	1.46	1.04	1.03
Fe^{3+}	0.06	0.00	0.14	0.01	0.07	0.01	0.00	0.08	0.00	0.00	0.00	0.00
Mn	1.44	2.34	1.53	2.43	2.96	2.48	2.68	3.12	2.45	2.63	1.41	1.42
Mg	0.02	0.04	0.01	0.10	0.06	0.16	0.12	0.04	0.17	0.11	0.02	0.02
Ca	3.97	2.84	3.76	2.00	2.21	2.56	1.64	2.14	2.56	1.72	3.43	3.51
Na	0.00	0.00	0.00	0.00	0.00	0.00	0.00	0.00	0.00	0.00	0.00	0.00
K	0.00	0.00	0.00	0.00	0.00	0.00	0.00	0.00	0.00	0.00	0.00	0.00
Total	16.00	16.00	16.00	16.00	16.00	16.00	16.00	16.00	16.00	16.00	16.00	16.00

	Biotite		Feldspar		Chlorite		Pyroxene		Epidote		Amphibole	
	Main South	North Pod	Within Main lode		Within Main lode		Unretrogressed skarn				Tremolite	Actinolite
SiO_2	36.74	42.55	45.16	41.37	27.93	28.37	53.14	52.73	38.59	39.54	53.28	51.88
TiO_2	1.25	0.54	0.01	0.01	0.02	0.11	0.00	0.01	0.01	0.29	0.01	0.03
Al_2O_3	18.38	12.77	35.55	33.75	22.27	22.79	0.08	0.57	32.32	27.27	2.67	4.20

(Continues)

TABLE 1 (Continued)

	Biotite		Feldspar		Chlorite		Pyroxene		Epidote		Amphibole	
	Main South	North Pod	Within Main lode		Within Main lode		Unretrogressed skarn				Tremolite	Actinolite
Cr_2O_3	0.03	0.01	0.00	0.00	0.00	0.06	−0.01	−0.01	−0.01	0.01	0.00	−0.01
FeO	16.51	8.42	0.05	0.12	20.63	20.94	7.92	7.33	2.54	7.18	6.34	13.57
MnO	0.65	0.40	0.00	0.10	1.38	1.24	2.49	3.27	0.22	0.47	1.34	3.71
MgO	12.62	21.84	−0.04	−0.03	17.80	17.49	12.52	12.46	−0.01	0.00	19.13	13.14
CaO	0.03	0.00	17.64	23.32	0.35	0.02	24.41	24.69	24.32	22.76	12.95	11.61
Na_2O	0.08	0.04	1.22	0.50	−0.01	0.01	0.00	0.03	0.01	0.00	0.20	0.23
K_2O	8.77	8.18	0.01	0.02	0.01	0.17	−0.01	0.01	0.01	−0.02	0.05	0.09
Total	95.05	94.75	99.60	99.15	90.37	91.21	100.54	101.10	98.00	97.49	95.96	98.46
Num ox	24.00	24.00	8.00	8.00	24.00	24.00	6.00	6.00	26.00	26.00	24.00	24.00
Si	6.01	6.67	2.08	1.93	2.81	2.83	1.99	1.96	6.24	6.55	8.07	7.99
Ti	0.15	0.06	0.00	0.00	0.00	0.01	0.00	0.00	0.00	0.04	0.00	0.00
Al	3.55	2.36	1.93	1.85	2.64	2.68	0.00	0.03	6.17	5.32	0.48	0.76
Cr	0.00	0.00	0.00	0.00	0.00	0.00	0.00	0.00	0.00	0.00	0.00	0.00
Fe^{2+}	2.26	1.10	0.00	−0.32	−4.13	−4.15	0.23	0.18	0.34	0.99	0.80	1.75
Fe^{3+}	0.00	0.00	0.01	0.32	5.87	5.90	0.01	0.05	0.00	0.00	0.00	0.00
Mn	0.09	0.05	0.00	0.00	0.12	0.11	0.08	0.10	0.03	0.07	0.17	0.48
Mg	3.08	5.10	0.00	0.00	2.67	2.60	0.70	0.69	0.00	0.00	4.31	3.01
Ca	0.00	0.00	0.87	1.16	0.04	0.00	0.98	0.99	4.22	4.04	2.10	1.92
Na	0.03	0.01	0.11	0.05	0.00	0.00	0.00	0.00	0.00	0.00	0.06	0.07
K	1.83	1.64	0.00	0.00	0.00	0.02	0.00	0.00	0.00	0.00	0.01	0.02
Total	17.00	17.00	5.00	5.00	10.00	10.00	4.00	4.00	17.00	17.00	16.00	16.00

Note: Fe^{3+} recalculation is based on ideal stoichiometry.

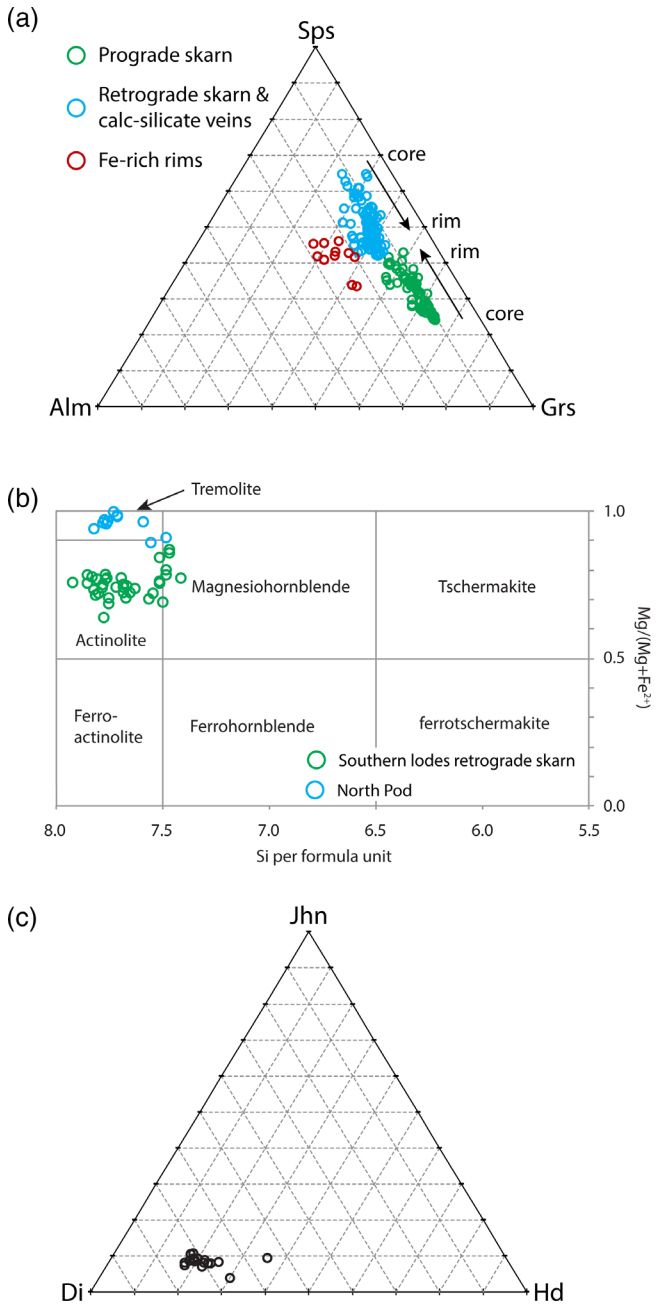

FIGURE 7 (a) Ternary plots of skarn garnet composition from Hera orebody. (b) Classification of amphiboles from Hera orebody based on Leeke et al (1997). (c) Ternary plot of pyroxene composition from Hera orebody

almandine and spessartine that varies between Xalm = 8.29–15.85, Xsps = 23.85–41.36 and Xgrs = 46.23–65.76 (Figure 7a). Core to rim chemical zonation involves compositionally homogenous grossular-rich cores (sometimes with calcite inclusions) that display sharp boundaries with spessartine enriched rims, which also host zoisite and tremolite inclusions (Figure 6b). A thin outer-rim of elevated Xalm, with decreased Xgrs and increased Xsps values, may be present. These elevated Xalm outer rim analyses are grouped with the latest-stage low-T hydrothermal alteration. Where remnant garnet–pyroxene-bearing carbonate skarn is preserved, with limited hydrous retrogression, garnet tends to have a less well-developed chemical zonation and is dominated by grossular-rich compositions. Fine-grained garnet in alteration haloes adjacent to calc-silicate veins within siliciclastic sedimentary rocks are generally enriched in spessartine and almandine components and vary from Xalm = 6.31–22.02, Xsps = 40.27–64.60 and Xgrs = 29.49–49.94.

Garnet within mineralized retrograde skarn, quartz–tremolite-rich veins and carbonate–tremolite-rich sulfide breccia fill has an elevated spessartine component, varying from Xalm = 5.94–18.69, Xsps = 41.76–64.65 and Xgrs = 23.85–44.27. Core to rim chemical zonation involves a smooth decrease in the Xsps ratio and sympathetic increase in Xgrs and Xalm values. A thin outer-rim of elevated Xalm with decreased Xgrs and Xsps values may be present.

Fine grained garnet associated with late-stage low-T chlorite–quartz–sulfide veins is relatively enriched in almandine component varying from Xalm = 20.03–28.57, Xsps = 33.27–45.28 and Xgrs = 27.02–42.94. Garnet of this composition are generally small, granular and with no discernable chemical zonation and appears to correlate with almandine-enriched garnet rims from all other settings.

Amphibole occurs in all stages of retrograde skarn and where it is developed in siliciclastic dominant parts of Hera (southern lodes) it varies from actinolite to manganoan-actinolite, Si p.f.u (per formula unit) ranges from 7.15 to 7.93 and XMg (Mg/Mg + Fe) ranges between 0.64 and 0.87 (Figure 7b). Manganese is elevated and ranges from 0.12 to 0.48 p.f.u. Lower Mn values tend to correlate with inclusions to garnet, while elevated Mn values tend to correlate with matted intergrowths of sulfide and amphibole external to garnet. Amphibole from the North Pod at Hera appears to have formed during both the prograde and retrograde skarn phases and is exclusively tremolite with Si p.f.u values ranging from 7.49 to 7.82, XMg values ranging from 0.89 to 1.0, and lower Mn values of 0.06–0.11 p.f.u. (Figure 7b). Amphibole associated with low-Fe sphalerite and nuggety gold in the Far West Lode is exclusively tremolite, with very low Mn values of 0.02–0.07 p.f.u.

Epidote is zoisite with $Fe^{3+}/(Fe^{3+}+Al)$ p.f.u values of 0.00–0.1596. Epidote from remnant garnet–pyroxene skarn has values plotting at the low Fe^{3+} end of this range. Allanite is visible optically, particularly in the North Pod, but was not analyzed as a part of this study. Late-stage, quartz vein hosted clinozoisite was not chemically analyzed as a part of this study.

Feldspar associated with anhydrous skarn is anorthite to bytownite with An (anorthite) (Ca/[Ca + Na + K]) values of 0.83–0.96. Orthoclase is present in association with low Fe-sphalerite and nuggety gold in the Far West lode. Albite (identified using XRD) is locally abundant in association with late stage bucky white quartz veins that crosscut the orebody.

Pyroxene from carbonate skarn is diopside (Figure 7c), although analyses display a manganoan component with Mn p.f.u ranging from 0.07 to 0.10.

Biotite from outer zone of alteration haloes around siliciclastic-hosted skarn veins and in the porphyroblastic biotite zone surrounding the orebody has an XMg (Mg/(Mg + Fe) ranging from 0.43 to 0.47. Biotite associated with tremolite/actinolite-rich retrograde skarn is more magnesian (XMg = 0.72). No biotite was analyzed from North Pod, although amphibole here trends to Mg-end member in the hydrous skarn from this zone and biotite is colorless to yellow brown in thin-section with low birefringence, consistent with the Mg-rich endmember. Biotite from the porphyroblastic halo around Hera orebody has a lower range in XMg values from 0.28 to 0.29.

Chlorite from late-stage hydrous alteration is predominantly ripidolite (ferroan clinochlore) with Si p.f.u values of 5.2–5.7 and Fe^{2+}+Fe^{3+} p.f.u values of 2.3–3.9. The lower values represent chlorite replacing inclusions in garnet.

4.2 | Stable isotopes

4.2.1 | S-isotopes

Nineteen sulfur isotope analyses were carried out from retrograde Au-bearing skarn that immediately postdates moderate-T retrograde skarn at Hera (seven analyses) and the moderate-T retrograde skarn in an adjacent mineralized zone (Kershaws zone;12 analyses) as part of the present study. These results are summarized in Table 2 and discussed below. The analytical procedure and tabulated results are included in the Supporting information.

S-isotope values from this study for Au-bearing low-Fe sphalerite-rich skarn at Hera average 5.4‰. Values for sphalerite range 5.1–6.0‰ (average 5.5‰ from six analyses) with a single value for galena–sphalerite of 4.6‰. The sulfur isotope values for the Kershaws zone are very similar and average 5.0‰. Pyrite from Kershaws has $\delta^{34}S$ values between 5.1 and 5.4‰ (average 5.2‰ from four analyses), sphalerite has values between 5.0 and 5.5‰ (average 5.2‰ from three analyses), galena has values of 4.2 and 4.3‰ and there are

TABLE 2 Sulfur isotope analyses carried out as part of the present study for Hera gold skarn and Kershaws lode

Location	Description	Chalcopyrite	Galena	Pyrite	Pyrrhotite	Sphalerite	Mixed sphalerite-galena
		$\delta^{34}S$‰ CDT					
Kershaws							
HRUD604—264.2 4 m	Veinlets of pyrite, and sphalerite–galena filling matrix		4.2	5.4		5.5	
HRUD604—284.1–284.35 m	Medium-grained chalcopyrite and pyrite as disseminations and veinlets, some sphalerite–galena also present.	5.4	4.3	5.1			
HRUD604—306.48–306.68 m	Medium-grained pyrite (early) with later sphalerite–minor galena			5.2		5.0	
				5.3		5.0	
HRUD604—320.61–320.79 m	Semi-massive pyrrhotite with lesser sphalerite and galena				5.5		4.5
Hera							
HRUD525—198.4–199.05 m	Semi-massive sphalerite with some galena (multiple grains sampled along a 0.65 m sulfide-rich interval)					5.1	4.6
						5.2	
						5.4	
						5.9	
						5.4	
						6.0	

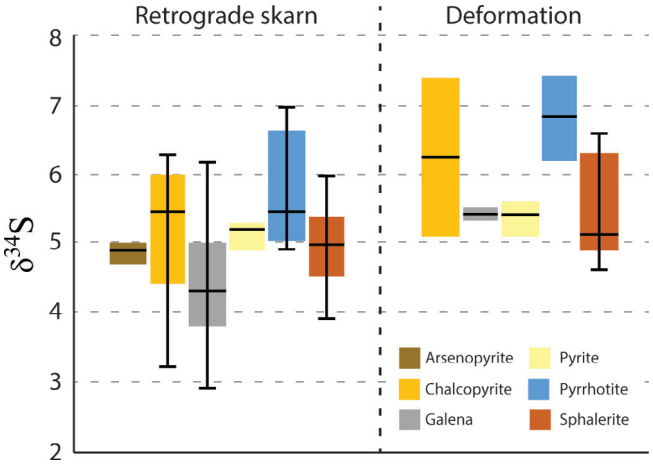

FIGURE 8 Box and whisker plot showing distribution of all sulfur isotope ($\delta^{34}S$) data for sulfides from mineralized zones at Hera. The plot includes data from David (2005), Mernagh (2008), Downes and Poulson (2018) and the present study

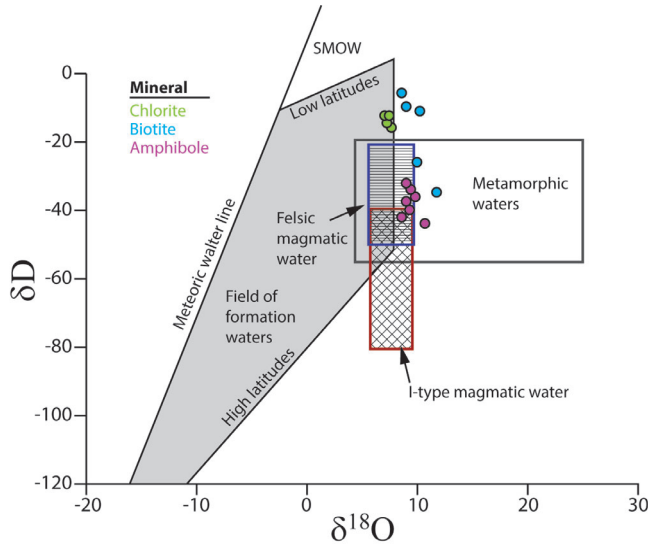

FIGURE 9 Calculated water δD–$\delta^{18}O$ values for the Hera orebody. See text for calculation details. Reference lines and boxes include, meteoric water line (Craig, 1961), felsic magmatic water (Taylor, 1992), primary I-type magmatic water and metamorphic water area (Hoefs, 2004)

single $\delta^{34}S$ values for chalcopyrite of 5.4‰, for pyrrhotite of 5.5‰ and sphalerite–galena of 4.5‰. Sixty-one additional sulfur isotope analyses are also available from previous studies by David (2005), Mernagh (2008) and Downes and Poulson (2018). The combined dataset from all studies plot in a tight cluster (Figure 8) between 2.9 and 7.4‰ (mean 5.0‰). The combined dataset of S-isotopes is subdivided in terms of retrograde skarn (both moderate and low-T) and deformation related sulfides. Although there is some overlap and the variation is subtle, deformation related (foliation hosted and late stage cross cutting) sulfides tend to be 0.5–1‰ heavier than the equivalent retrograde skarn phase sulfides (Figure 8).

4.2.2 | O—H isotopes

Water δD–$\delta^{18}O$ values were determined using δD and $\delta^{18}O$ values for tremolite (from mineralized retrograde skarn), biotite, chlorite (both from the host rocks adjacent to skarn) and clinozoisite (from late cross-cutting veins) using estimated temperatures of last equilibration and adjusted for their mineral composition and are presented in Figure 9 (see Suzuoki and Epstein, 1976; Graham *et al.*, 1980; Matthews *et al.*, 1983; Graham *et al.*, 1984; Graham *et al.*, 1987; Fortier and Giletti, 1991; Vennemann and O'Neil, 1996; Cole and Ripley, 1999 and Saccocia *et al.*, 2009). The estimation of water δD-$\delta^{18}O$ values from biotite can be problematical. Biotite–water exchange experiments of Suzuoki and Epstein (1976) show a systematic decrease in the hydrogen isotope mineral–water fractionation factor ($10^3\ln\alpha$) from 850 to 400°C. The experimental findings of Vennemann and O'Neil (1996) indicated a pronounced increase in $10^3\ln\alpha$ for temperatures of ≤400°C. The inflection point between these two trends is between 350 and 400°C, although there is a mismatch in the compositions of biotite used in these experiments. We have used a uniform value of −38.1 for $10^3\ln\alpha$ to estimate water δD values for water–biotite pairs estimated to have exchanged in the range 300–400°C to accommodate this inflection point and to avoid extrapolating the results of Suzuoki and Epstein (1976) below their experimentally determined range. An XMg value of ~0.80 was determined for Mg-rich biotite from the skarn margin (from microprobe data), although biotite in the most magnesian assemblages, particularly from North Pod, may have values closer to XMg = 1. Extrapolation of the Suzuoki and Epstein equilibria to 300°C for Mg-rich biotite analyzed in this study result in $10^3\ln\alpha$ values of −57 and water δD values greater than +9. Such values are regarded as implausible when compared to δD values for waters calculated from other minerals in this study.

Calculated water δD–$\delta^{18}O$ values for Hera form a tight array within retrograde skarn minerals (tremolite) within massive sulfide breccia having δD–$\delta^{18}O$ values plotting in a field typically associated with magmatic or metamorphic water (Figure 9). In addition, there is a trend toward increasing δD values, with very minor changes to $\delta^{18}O$ values, for lower temperature minerals developed in the margin to the orebody (i.e., biotite) or in later paragenetic stages (clinozoisite–chlorite) (Figure 9).

4.3 | U–Pb geochronology

Sensitive high-resolution ion microprobe (SHRIMP), isotope dilution thermal ionization mass spectrometry (ID-TIMS) and *laser ablation* inductively coupled plasma mass spectrometry (LA-ICP-MS) U–Pb dating was carried out on titanite from three different settings at Hera; (1) quartz–ilmenite–titanite vein that cross-cuts prograde skarn in the Far West lode (Sample JAF01), (2) remnant low-T retrograde, K-feldspar-altered skarn fragments associated with low-Fe sphalerite–titanite–Au-rich breccia (Sample JAF02) and, (3) thrust fault-related late-stage quartz–chlorite–titanite veins that crosscut the orebody (Samples JAF03 and JAF04). Grains of titanite 100 μm or greater in diameter (some broken from cm-scale grains) were liberated by hand-crushing. Titanite fragments from all samples are transparent and colorless, with occasional zones of fluid inclusions. Back-scattered electron images show that all fragments lack discernible zonation, reflecting the chemically homogeneous nature of the grains. Detailed analytical methods and results are outlined in the Supporting information.

Twenty-seven LA-ICP-MS U–Pb analyses were carried out on titanite grain fragments from sample JAF01. Measured U/Pb ratios were calibrated via measurements of the reference titanite MKED1 (Spandler *et al.*, 2016).

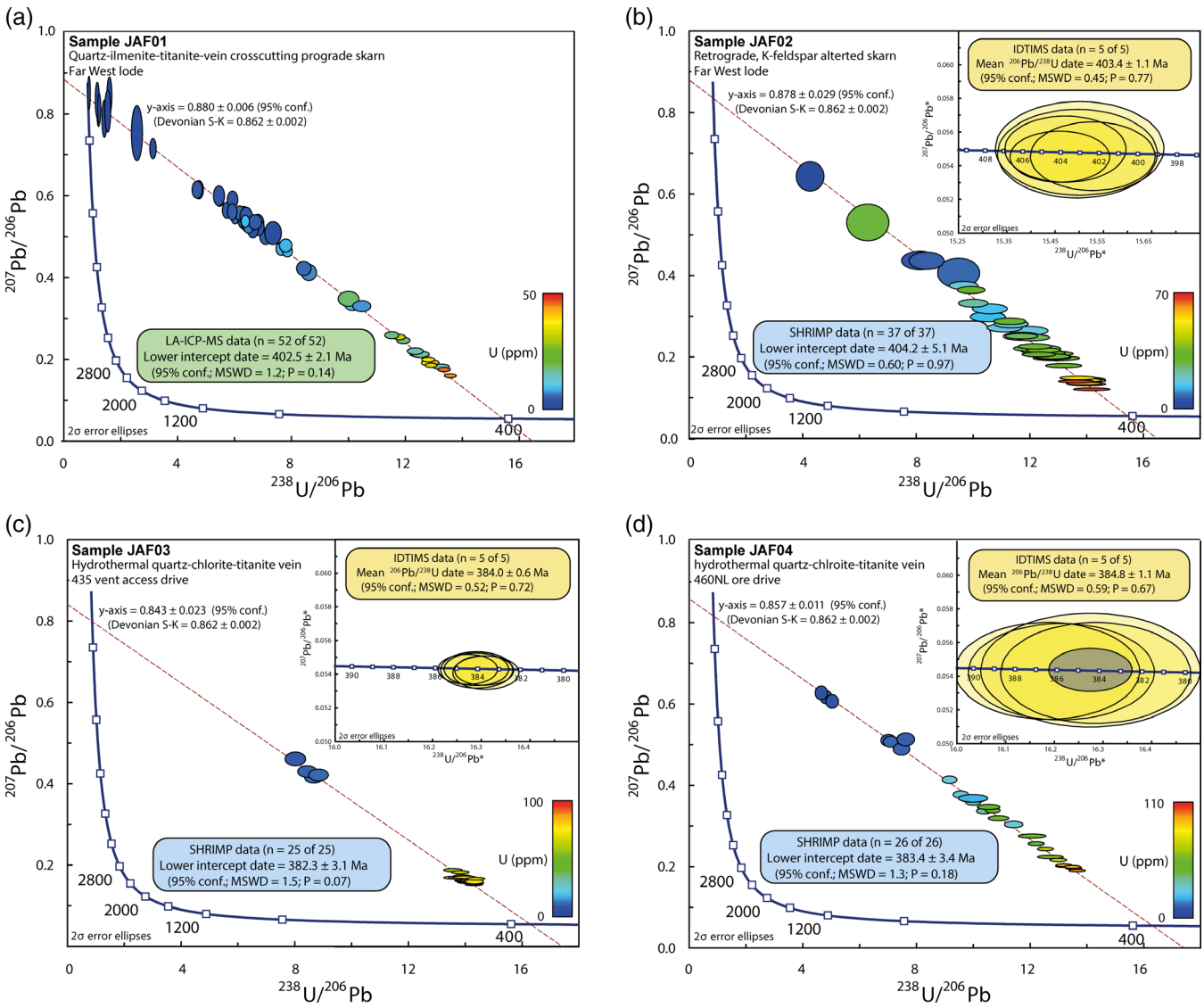

FIGURE 10 Tera-Wasserburg plots showing U–Pb results for titanite samples and correlative photographs of actual dated samples from (a) Au-rich mineralization in the Far West lode in the Hera mine; (b) a quartz–ilmenite–titanite vein cross-cut garnet-rich skarn in the far west lode at Hera mine; (c and d) from hydrothermal quartz veins that partially dismember the Hera orebody. SHRIMP or LA-ICP-MS data is displayed in the main panel, and where collected ID-TIMS data in the inset. All data are plotted with 2 sigma uncertainties. Individual SHRIMP and LA-ICP-MS analyses are colored by U content. All ages are interpreted as the timing of titanite crystallization and/or closure of its U–Pb isotopic system

TABLE 3 Summary of titanite U–Pb dating results for Hera

Sample no. (timing relationship)	Age (Ma, ±95% CI)	MSWD	*p*	No. of analyses	Method
JAF01 (vein cross-cutting prograde skarn)	402.3 ± 3.6	1.3	.11	27	LA-ICP-MS
JAF02 (retrograde skarn phase)	404.2 ± 5.1	0.60	.97	37	SHRIMP
JAF02 (retrograde skarn phase)	403.4 ± 1.1	0.45	.77	5	IDTIMS
JAF03 (GA2615454) (late-deformation vein)	383.4 ± 3.4	1.3	.18	26	SHRIMP
JAF03 (GA2615454) (late-deformation vein)	384.8 ± 1.1	0.59	.67	5	IDTIMS
JAF04 (GA2615455) (late-deformation vein)	382.5 ± 3.1	1.5	.07	25	SHRIMP
JAF04 (GA2615455) (late-deformation vein)	384.0 ± 0.6	0.52	.72	5	IDTIMS

The dataset is portrayed on a Tera-Wasserburg diagram (Figure 10a). The Pb-isotopic systematics for this sample suggests that the U–Pb system is undisturbed (within the precision of the analyses) and that the Devonian lower intercept represents the true age of titanite crystallization and/or U–Pb isotopic closure. This sample gave a date of 402.3 ± 3.6 Ma for the quartz–ilmenite–titanite vein that crosscuts high-T prograde skarn in the Far West lode (Table 3).

Between 25 and 37 SHRIMP U–Pb analyses were carried out on titanite fragments from sample JAF02, JAF03 and JAF 4 on the SHRIMP IIe instrument at Geoscience Australia, Canberra. All analyses were characterized by low U contents (2–107 ppm, median 35 ppm). Sample JAF03 has a bimodal distribution with some grains having very low U (7–11 ppm). Consequently, SHRIMP analysis for this sample targeted a subset of grains with higher U (57–93 ppm, median 75 ppm). By contrast, titanite from sample JAF04 had a wider range of U values (6–107 ppm, median 39 ppm). For both samples, Th/U is uniformly low (0.02–0.04, median 0.03 and 0.03–0.07, median 0.05 respectively). Sulfide-Au hosted skarn sample JAF02, is characterized by U values (2–69 ppm, median 27 ppm) that are mostly lower than for JAF03 and JAF04, but Th/U is markedly higher (0.15–1.25, median 0.80). Common ^{206}Pb as a proportion of total ^{206}Pb is high (8–73%, median 20%) for this sample as is usual, in Phanerozoic titanite, and displays a largely predictable relationship with U content. Measured titanite U/Pb ratios were calibrated via measurements of reference titanite MKED1 (Spandler *et al.*, 2016) with no correction for common Pb. The results are portrayed on Tera-Wasserburg diagrams (Figure 10a–d) with each dataset defining a statistically coherent discordia array (*p* exceeds .05 in all three cases). In all three cases, the y-intercept of the discordia is indistinguishable from the range of Devonian bulk-Earth ^{207}Pb/^{206}Pb values as modeled by Stacey and Kramers (1975): that is, 0.864 at c. 419 Ma through 0.860 at c. 359 Ma, and direct Pb-isotope measurement on 11 galena samples from the Hera mine averaging 0.863 (Downes and Poulson, 2018). This suggests that each of the U–Pb systems are undisturbed (within the precision of the analyses) and that each Devonian lower intercept represents the true age of titanite crystallization (and/or U–Pb isotopic closure). Sample JAF02 gave an age of 404.2 ± 5.1 Ma for the sulfide-rich skarn-hosted sample, while JAF03 and JAF04 gave dates of 383.4 ± 3.4 Ma and 382.5 ± 3.1 Ma (respectively) for the quartz-rich veins hosted by crosscutting, thrust related structures. These results are summarized in Table 3.

Titanite grains from samples JAF02, JAF03 and JAF04 were reanalyzed at the Boise State University Isotope Geology Laboratory using ID-TIMS, to obtain more precise U–Pb dates, and to evaluate the accuracy of the MKED1-based calibration of ^{206}Pb/^{238}U used in the SHRIMP dating. Five titanite fractions with similar chemical composition to those analyzed via SHRIMP were analyzed from each of the three samples. Common Pb corrections were made using measured ^{204}Pb and the two-stage Pb isotope evolution model of Stacey and Kramers (1975) at the nominal sample age. In all three cases, the five analyses for each sample are indistinguishable within their analytical uncertainties and define weighted mean ^{206}Pb/^{238}U dates well within uncertainty of the lower-intercept dates determined from the SHRIMP-derived discordia arrays (Figure 10b–d; Table 3). Sample JAF02 gave an age of 403.4 ± 1.1 Ma, while JAF03 and JAF04 gave dates of 384.0 ± 0.6 Ma and 384.8 ± 1.1 Ma (respectively). These results are summarized in Table 3. The excellent agreement between all three pairs of results confirms the accuracy of the MKED1-based calibration of SHRIMP-determined ^{238}U/^{206}Pb in the unknowns. All ID-TIMS and SHRIMP results from statistically coherent age groupings and the SHRIMP and ID-TIMS data for each sample are within uncertainty of each other (Table 3).

4.4 | Ar–Ar geochronology

Ar–Ar dating was carried out at the University of Melbourne noble gas laboratory, on two biotite separates

from biotite-rich schist developed around the margins of the Hera orebody (samples NSW34-2 and NSW34-3). Detailed analytical methods and results are outlined in the Supporting information. Age spectra for both separates are presented in Figure 11 and results are summarized in Table 4. The spectra are characterized by anomalously young apparent ages for the initial heating step (339.1 ± 1.2 Ma for NSW34-2, 346.0 ± 0.6 Ma for NSW34-3). Followed by a gradual increase from ~385 to ~389 Ma for low to intermediate steps (385.62 ± 0.45 Ma to 388.87 ± 0.41 Ma for NSW34-2; 385.48 ± 0.33 to 388.41 ± 0.37 Ma, for NSW34-3). The mid- to high-temperature steps yield identical plateau ages of 390.03 ± 0.23 Ma (59.5% ^{39}Ar release for NSW34-2) and 389.60 ± 0.23 Ma (57.2% ^{39}Ar release, NSW34-3).

The anomalously low age yielded by the first heating step of each aliquot is most likely an artefact of argon recoil. The "staircase" portion of the spectra (385–389 Ma), may reflect either partial resetting at or after 385 Ma by a later thermal event, and/or be an artefact of argon recoil. Regardless, the mid- to high-temperature heating steps yield extremely concordant results (both within and between aliquots), and as such the plateau ages are considered to reflect the cooling age of the biotite or the crystallization age if crystallization occurred ≤300° C (i.e., below biotite ^{40}Ar/^{39}Ar closure temperature; McDougall and Harrison, 1999).

Downes and Phillips (2018) reported ^{40}Ar/^{39}Ar step-heating age spectra for undeformed muscovite laths and rosettes intergrown with sulfides (galena–sphalerite–pyrrhotite–chalcopyrite) at Hera (drill hole HRD032; 514 m). The muscovite showed a well-defined plateau age of 381.9 ± 2.2 Ma. Table 4 summarizes the ^{40}Ar/^{39}Ar results from the two studies.

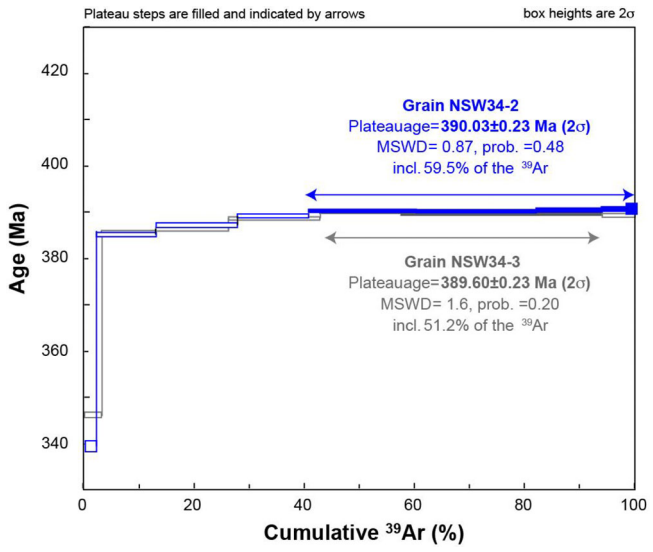

FIGURE 11 Ar–Ar age spectra for two samples of biotite sampled from the foliation that envelopes the Hera orebody

5 | DISCUSSION

5.1 | Hera mineral chemistry, stable isotopes, and fluid evolution: A magmatic-related distal skarn?

Distinctive petrographic and mineral chemical features of the Hera orebody (e.g., sub-calcic garnet, pronounced Mn and prevalence of Fe^{2+} in skarn minerals, as well as low Mo in scheelite) in combination with the absence of a thermal aureole are consistent with primary mineralization at Hera being related to the retrograde phase of a reduced (pyrrhotite-stable) distal Zn-skarn system as described by Einaudi *et al.* (1981) and Meinert (1992).

Prograde and retrograde skarn mineral assemblages vary from Ca–Mg enriched in the north (diopside, tremolite, phlogopite, talc, anorthite), to comparably Ca–Fe enriched in the south (garnet, actinolite, biotite). This change in mineralogy in part reflects changing host lithology and ultimately changing bulk chemistry of the reactive sequence, with Mg enriched carbonate-bearing sequences most prevalent in the north and exclusively siliciclastic, comparably Fe-enriched (siltstone-rich) sequences in the south. Another factor in the complex mineralogy and mineral chemistry of the Hera distal skarn is the inferred low XCO_2 and potential decrease in XCO_2 during skarn evolution. Carbonate preservation is poor, and it has been mostly consumed to form calc-silicate minerals during skarn formation. Figure 12 illustrates the T–XCO_2 stability region for both prograde and retrograde mineral associations most applicable to the Mg-enriched calc-silicate assemblages of the northerly lodes (Far West and North Pod) of the Hera skarn.

TABLE 4 Summary of mica Ar–Ar results for Hera

Sample	Age (Ma, ±95% CI)	MSWD	*p*	% ^{39}Ar release	Mineral
HRD018 (Downes and Phillips, 2018)	381.9 ± 2.2	1.4	.24	65.5	Muscovite
NSW34-2	390.03 ± 0.23	0.87	.48	59.5	Biotite
NSW34-3	389.60 ± 0.23	1.6	.20	57.2	Biotite

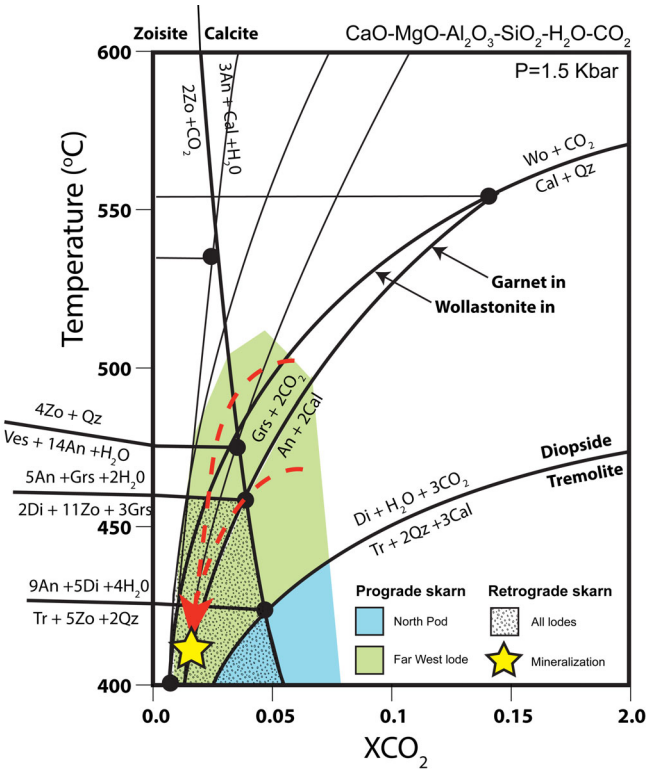

FIGURE 12 Schematic isobaric T–X(CO_2) phase-equilibrium diagram for the CaO–MgO–Al_2O_3–SiO_2–H_2O–CO_2 system, modified after Rossetti and Tecce (2008). Colored fields depict the potential stability fields of the North Pod and Far West lode during the prograde and retrograde skarn phases

Changing mineral parageneses imply the garnet–pyroxene ± wollastonite (see Figure 4) bearing prograde skarn phase of the Far West lode initially developed at $XCO_2 \geq 0.05$ in the field of calcite stability (preserved mostly as inclusions in garnet), but XCO_2 rapidly decreased into the field of zoisite stability in the presence of garnet and diopside. Finally, decreasing temperature from south to north along the length of the Hera orebody (and potentially up plunge in the North Pod) can account for the loss of garnet and pyroxene and prevalence of amphibole in the upper North Pod. Peak prograde skarn temperature potentially varied from 400 to 430°C for the upper North Pod and 430 to 500°C for the Far West lode (Figure 12). Decreasing temperature and mineralizing fluid ingress during the retrograde skarn phase also resulted in hydrous, amphibolite-rich associations and the replacement of peak garnet–pyroxene-rich associations in Far West lode during retrograde skarn development (Figure 12). Temperature ultimately decreased to <350°C where chlorite-rich epizonal mineral assemblages formed.

The sulfur isotopic characteristics of the Hera orebody are unusual in the context of the Cobar Basin. Variation in $\delta^{34}S$ is narrow and low (2.9–7.4‰) consistent with $\delta^{34}S$ for granitic rocks (Hoefs, 2004), while most other Cobar Basin orebodies vary between 5 and 12‰ (some up to 20‰). Whole rock $\delta^{34}S$ for selected Devonian intrusive and volcanic rocks from the Cobar Basin range between 4 and 6.2‰ (Downes and Poulson, 2018), while reduced seawater sulfate associated with the Cobar Basin should be 10–15‰ (Seccombe *et al.*, 2017). The narrow range and low S-isotope values, for Hera are most consistent with a Devonian intermediate to felsic igneous reservoir and do not support the interpretation that significant sulfur was sourced from a fractionated Early Devonian seawater sulfate reservoir. Interestingly, when sulfur isotopes for Hera are divided into those associated with skarn and those associated with overprinting deformation, $\delta^{34}S$ for the latter is consistently 0.5–1‰ higher. This increase in $\delta^{34}S$ may reflect input of heavier sulfur form the Cobar Basin sedimentary rocks during deformation and basin inversion.

Calculated water δD–$\delta^{18}O$ values for retrograde skarn minerals (tremolite) from within the massive sulfide breccia at Hera form a tight array, being typical of magmatic or metamorphic water (Figure 9). There is trend toward increasing δD values, with minor shift in $\delta^{18}O$ values for lower temperature minerals developed in the altered, siltstone-rich margin to the orebody (i.e., biotite) and/or in later paragenetic stages (chlorite) (Figure 9). Calculated δD–$\delta^{18}O$ values for some retrograde skarn phase biotite in the wall rocks to the Hera orebody, as well as overprinting deformation related biotite and chlorite defining the foliation around the orebody fall outside the field of magmatic and metamorphic waters from Taylor (1997) and require an external source of unexchanged waters to account for the observed trend. It is likely that original magmatic or metamorphic water of the retrograde skarn phase underwent progressive mixing or dilution late in the skarn forming event and more likely during the early stages of deformation by unexchanged waters with δD–$\delta^{18}O$ values typical of low latitude (tropical) meteoritic waters around the margins of the massive sulfide breccia—this is consistent with the paleogeographic setting of the Cobar Basin during the late Silurian–Early Devonian (see Domeier and Torsvik, 2014).

The features of skarn mineralization, including the preservation of prograde, high-T skarn assemblages hosted within sub-greenschist facies basin sedimentary rocks (Fitzherbert *et al.*, 2017a, b) and thermal changes reflected by changing skarn mineralogy (south to north and down plunge) at the Hera orebody are inconsistent with the current model for formation of Cobar-type deposits through deep burial and regional-scale ingress of basement and basin derived fluids during basin inversion (Stegman, 2001). Although no direct link to magmatic

rocks has been established at Hera, the features listed below are suggestive of magmatic heat and fluid/metal/sulfur input(s) to the Hera mineral system:

- Rapid changes in skarn mineralogy and the large thermal contrast between distal basin and skarn mineralization reflecting proximity to major flow channels, possibly reflected by the pyroxene-rich Far West Lode (see Einaudi *et al*., 1981; Meinert, 1992; Fitzherbert *et al*., 2017a, b).
- $\delta^{34}S$ values form a very tight cluster between 2.9 and 7.4‰ (average 5.0‰) consistent with Devonian magmatic sulfur from the Cobar region.
- δD–$\delta^{18}O$ values are consistent with progressive mixing or dilution of original magmatic/metamorphic waters within the Hera deposit by unexchanged waters typical of low latitude meteoritic waters.
- Pb–model ages of 412–397 Ma for galena from the Hera orebody (Downes and Poulson, 2018) agree well with U–Pb age of 403.4 ± 1.1 for hydrothermal titanite from Zn–Au-skarn at Hera (i.e., Pb-source age and the age of mineralization are the same). Such a scenario can be most simply explained by the presence of a ≥ 403 Ma distal magmatic influence.
- Fitzherbert *et al*. (2017a, b) estimated sub-greenschist facies burial metamorphic conditions of T = 200–250°C for unaltered host rocks at Hera, with an increase to peak temperatures of ≥400°C (potentially ≤500°C) for the anhydrous prograde skarn associated with the orebody. This 150–200°C (potentially 250–300°C) thermal contrast between host rocks and skarn is inconsistent with metamorphic-reaction skarn, and more consistent with a distal igneous-metasomatic skarn (see Einaudi *et al*., 1981).

5.2 | Timing of mineralization within a regional tectonic framework

High precision geochronology suggests the Hera orebody has had a protracted history of mineralization/remobilization from initial fault controlled distal base-metal skarn at ≥403 Ma, to Zn–Au-rich mineralization at 403 Ma, inversion initiation and ductile foliation development and ore remobilization/new mineralization at c. 390 Ma, brittle reverse faulting with orebody dismemberment and late inversion-related remobilization/mineralization at 381 Ma. The Cobar Basin has the highest metal endowment of the Siluro-Devonian basins in New South Wales (see Greenfield *et al*., 2015; updated figures for Cobar Basin, Seccombe *et al*., 2017). Perhaps a key to this endowment is the plurality of mineralization along the major eastern fault corridor, Rookery Fault. Rather than relying on a single ore forming event it is likely that the Hera deposit developed through successive mineralizing, remobilization/concentration events over ~20 Ma.

A generalized model for the opening of the Cobar Basin involves a rift phase from 420 to 415 Ma followed by a sag phase between 415 and 406 Ma (van der Wielen and Glen, 2008, Glen *et al*., 2016) and possibly as late as

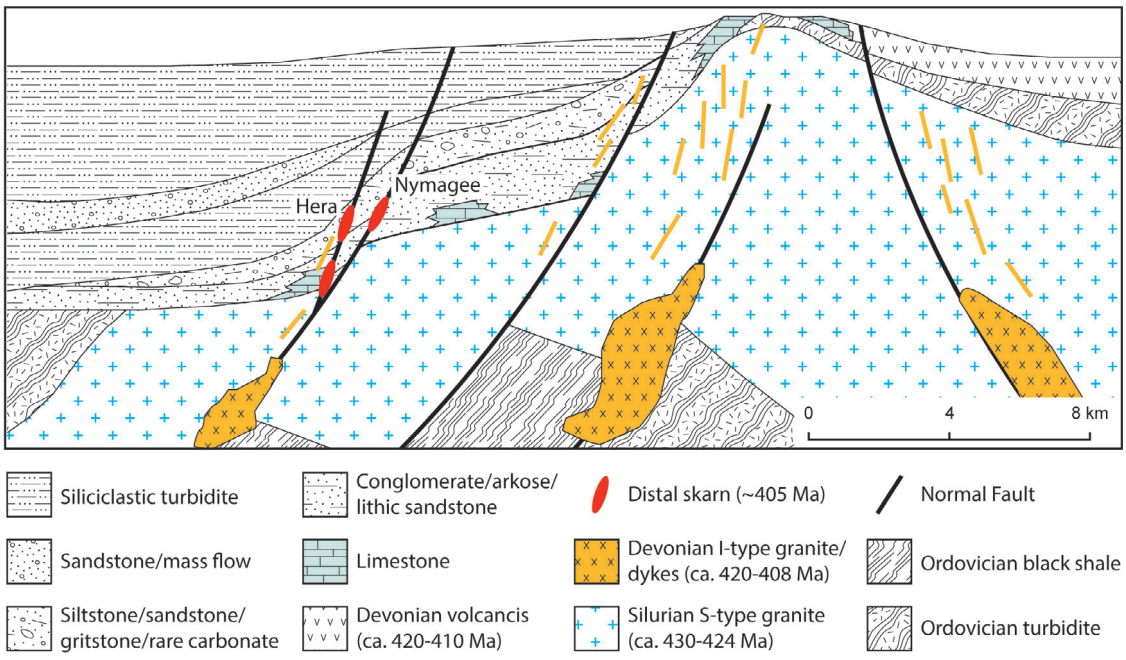

FIGURE 13 Interpretive NE facing cross section of the "late sag phase" southern Cobar Basin at 410–400 Ma

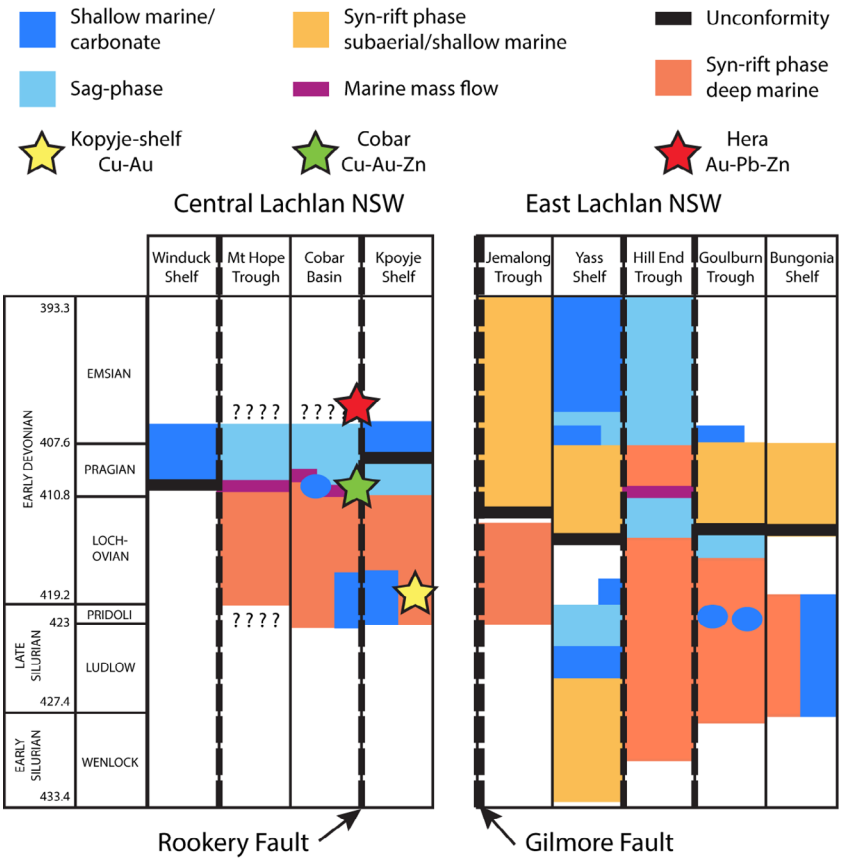

FIGURE 14 Comparative time–space plot between the central and eastern Lachlan Orogen (modified after Fitzherbert *et al*., 2019). Mineralizing intervals for Kopyje shelf Cu–Au and Cobar Cu–Au–Zn based on Fitzherbert *et al*. (2019) and Hera Au–Pb–Zn based on this study. Time–space relationships for Yass Shelf, Hill End Trough, Goulburn Trough and Bungonia Shelf are from Thomas and Pogson (2012). Time–space relationships for the Jemalong Trough are from Lyons *et al*. (2000). Time–space relationships for the central Lachlan Orogen are from Glen (1987, 1994) and Downes *et al*. (2016). Relative timing of central Lachlan Orogen time–space relationships has been adjusted according to paleontological determinations of Mathieson *et al*. (2016)

400 Ma (Parrish *et al*., 2018). A recent review of conodont fauna in limestone of the Cobar Basin by Mathieson *et al*. (2016) places allochthonous limestone blocks hosted within a rift to sag phase (Biddabirra Formation; Figure 1) transitional facies in the Pragian at c. 410–408 Ma. An estimated 6–8 km of sag phase turbidite overlies the Biddabirra Formation (Glen, 1987). Deposition in the flanking shallow-water sequences (Winduck Shelf in the west and Kopyje Shelf [Yarra Yarra Creeek Group] in the east; Figure 1) continued into the Emsian c. 406 Ma (Mathieson *et al*., 2016). Bull *et al*. (2008) and Downes *et al*. (2016) dated rift-related, deep-water A-type volcanics (Rast Trough; Figure 1) at c. 412–409 Ma (Figure 1). The Hera skarn may have formed due to fault movements during the later stages of sag phase of the basin deposition, but magmatic rocks this young are so far undiscovered in the Cobar Basin (see Figure 13 for an interpreted cross section through the ca. 410–400 Ma late sag phase Cobar Basin).

The Rookery Fault is a splay off a crustal-scale master fault system, the Gilmore Fault (Glen, 1982). The Gilmore Fault separates two tectonic entities in New South Wales; the central Lachlan Orogen (host of the Cobar Basin) and the eastern Lachlan Orogen. Basins (Jemalong Trough; Figure 16) preserved in the eastern Lachlan Orogen directly adjacent to the Gilmore Fault record a protracted history of rifting and bimodal magmatic activity through the Pragian to the middle Emsian c. 410–400 Ma (Lyons *et al*., 2000; Raymond *et al*., 2000, 2000a). Further east (Yass Shelf, Hill End Trough, Goulburn Trough and Bungonia Shelf; Figure 14) voluminous I-type silicic magmatism continued well into the early Emsian and was followed by a period of quiescence and limestone accumulation until c. 400 Ma (e.g., Thomas and Pogson, 2012). We propose that far-field forces associated with Pragian and potentially early Emsian tectonism in the eastern Lachlan Orogen have been translated as movement along the Gilmore and linked Rookery Fault systems. Distal skarn developed within the Cobar Basin, likely associated with limited magmatism that was focused along this crustal-scale fault system. Fault-focused magmatism has occurred during prior movements on the Gilmore and Rookery Faults, including the Avenall Metabasic Complex (415–411 Ma; Cairns, 1997; Kositcin, 1999) that stitches the Gilmore Fault to the south of Cobar, as well as fault localized dykes/plutons (415–410 Ma; Downes *et al*., 2016; Jones *et al*., 2020) within the Rookery Fault system. It is credible that extension reflected by continued rifting and magmatism in the east Lachlan Orogen from 415 to 400 Ma translated into periodic movements and fault focused diking/plutonism on the

predominantly strike-slip Gilmore-Rookery Fault system.

Inversion of the Cobar Basin is thought to have occurred between 400 and 380 Ma (Glen *et al*., 1992). Our dating suggests that basin inversion progressed from ductile deformation and foliation generation c. 390 Ma to brittle thrusting at c. 384 Ma. There is certainly evidence of sulfide and Au deposition post-dating the foliation at Hera but based on the above evidence it is likely the Ar–Ar white mica age of 381.9 ± 2.2 Ma for mineralization (Downes and Poulson, 2018) represents a cooling age toward the end of the Tabberabberan Orogeny inversion. In saying this, Pb–Zn mineralization is clearly associated with the Tabberabberan Orogeny and movement of basinal fluids within other orebodies of the Cobar Basin (e.g., Endeavor mine; Lawrie and Hinman, 1998; Sun *et al*., 2000). The late-stage Pb–Zn mineralization at Hera may potentially be of this generation.

5.3 | Recognition of a distal skarn district

The link between faults, stratigraphy and mineralization at Cobar has been discussed before (e.g., Berthelsen, 2006), but the relatively recent development of the Far West lode and the North Pod at Hera has uncovered a previously unknown skarn altered, sandstone/gritstone/carbonate-bearing stratigraphy. In light of the newly described skarn association at Hera, reconnaissance studies have revealed that skarn mineralization in the south-eastern Cobar Basin is relatively wide-spread (Fitzherbert *et al*., 2017a, b). Garnet–anorthite-rich skarn alteration is associated with the Cu-rich Nymagee deposit, 5 km north of Hera (Fitzherbert *et al*., 2017a, b) and garnet-rich calc-silicate veins are present at the Happy Jacks prospect a further ~2.5 km north (along strike) from Nymagee (Fitzherbert *et al*., 2017a, b). Mineralization and garnet-rich skarn associations are also recorded to the south of Hera, at Hebe prospect (Fitzherbert *et al*., 2017a, b). This distribution of skarn and skarn veins is associated with the same fault system and at the same stratigraphic level, being controlled by a single (>7.5 km strike length) horizon adjacent to a major basin margin fault. Allochthonous carbonate blocks are also present along the western margin of the basin. These include the Norma Vale prospect, where pyroxene-rich skarn is associated with Cu mineralization at the base of a large allochthonous limestone block within the Shume Formation (Figure 1; Fitzherbert *et al*., 2017a, b). The Shume Formation and correlative Biddabirra Formation both host allochthonous limestone and are stratigraphically higher than the Hera–Nymagee allochthonous horizon suggesting there are a number of prospective allochthonous rock packages within the deep-water Cobar Basin stratigraphy. The lower Cobar Basin sequences comprise shallow water reef to shelf sequences developed at the early-stage of rifting. These lower basin sequences host abundant conglomerate and carbonate, and with a shift in paradigm to a skarn mineral system model these shelf sequences become highly prospective for skarn mineralization.

6 | CONCLUSIONS

The Hera orebody preserves primary distal skarn mineralization and has petrographic and mineral chemical characteristics consistent with a reduced, polymetallic siliciclastic/calcic skarn. Skarn mineralization in the Cobar Basin occurs where long-lived basin margin fault systems intersected stratigraphy that contains coarse-grained sandstone/gritstone horizons and rare carbonate clasts. The O-H isotopic characteristics of the Hera orebody are consistent with magmatic/metamorphic water that mixed with cooler low latitude basinal fluids, while sulfur isotopic characteristics imply mixed magmatic/basin sulfur input. The coincidence of the Pb-model ages for Hera with U–Pb titanite ages for mineralization implies the early Emsian ≥405–402 Ma was a period of movement along the Rookery Fault. This movement, in conjunction with fault focused magnatism likely gave rise to structurally hosted distal skarn at Hera. It is plausible that multiple movement events and potentially varying magmatic/basin metal input has resulted in the complex, polymetallic nature of the Hera skarn. A ductile foliation associated with basin inversion is dated at c. 390 Ma and the Hera orebody was dismembered by brittle faulting at c. 384 Ma. Late-stage Pb–Zn mineralization that cross-cuts the foliation is present at Hera, has been dated at c. 381 Ma and may reflect further basin derived mineralization during post-orogenic relaxation. Skarn mineralogy has been described at several prospects and deposits up to 7 km away from the Hera orebody implying that a larger and highly prospective distal skarn system occurs in the region.

ACKNOWLEDGMENTS

This study was undertaken as part of the NSW Governments New Frontiers Initiative. Simon Poulson is thanked for undertaking the sulfur-isotope analyses at the Nevada Stable Isotope Laboratory, University of Nevada, Reno, USA. Publication is with the permission of the Executive Director Geological Survey of New South Wales. Kathryn Waltenberg publishes with the permission of the Chief Executive Officer, Geoscience Australia.

The authors would like to thank Dr Nancy Vickery and two unnamed reviewers for their constructive suggestions that greatly improved the manuscript.

DATA AVAILABILITY STATEMENT

The data that supports the findings of this study are available in the supplementary material of this article.

ORCID

Joel A. Fitzherbert https://orcid.org/0000-0003-2194-6949
Peter M. Downes https://orcid.org/0000-0002-3979-1845
Corey Wall https://orcid.org/0000-0002-3385-5721

REFERENCES

Berthelsen, R. (2006) The Cobar goldfield—a variation of a theme. In: Lewis, P.C. (Ed.) *Mineral Exploration Geoscience in NSW, Mines and Wines 2006 Conference, Extended Abstracts*. Sydney: Sydney Mineral Exploration Discussion Group, pp. 71–78.

Bull, K.F., Crawford, A.J., McPhie, J., Newberry, R.J. and Meffre, S. (2008) Geochemistry, geochronology and tectonic implications of late Silurian–early Devonian volcanic successions, central Lachlan Orogen, New South Wales. *Australian Journal of Earth Sciences*, 55, 235–264.

Cairns, B.J. (1997) Geology of the Adelong Goldfield. BSc Hon Thesis, Australian National University, Canberra (unpubl.).

Cole, D.R. and Ripley, E.M. (1999) Oxygen isotope fractionation between chlorite and water from 170 to 350°C: a preliminary assessment based on partial exchange and fluid/rock experiments. *Geochimica et Cosmochimica Acta*, 63, 449–457.

Craig, H. (1961) Isotopic variations in meteoric waters. *Science*, 133, 1702–1703.

David, V. (2005) Structural Setting of Mineral Deposits in the Cobar Basin. PhD thesis, University of New England, Armidale (unpubl.).

David, V. (2006) Cobar Superbasin System metallogenesis. In: Lewis, P.C. (Ed.) *Mineral Exploration Geoscience in New South Wales, Extended Abstracts*, pp. 39–51. Mines and Wines Conference 2006, Cessnock NSW, SMEDG (Sydney Mineral Exploration Discussion Group).

Domeier, M. and Torsvik, T.H. (2014) Plate tectonics in the late Paleozoic. *Geoscience Frontiers*, 5, 303–350.

Downes, P.M. and Phillips D. (2018) $^{40}Ar/^{39}Ar$ geochronology of three samples from mineralised zones in the Nymagee project area: preliminary results. Geological Survey of New South Wales Report GS2018/0164. https://search.geoscience.nsw.gov.au/.

Downes, P.M. and Poulson, S.R. (2018) Isotope signatures of selected Silurian to Devonian mineral systems in the Nymagee area, central Lachlan Orogen, New South Wales. *Quarterly Notes of the Geological Survey of New South Wales*, 151, 1–35. https://search.geoscience.nsw.gov.au/product/9223.

Downes, P.M., Blevin, P.L., Armstrong, R., Simpson, C.J., Sherwin, L., Tilley, D.B. and Burton, G.R. (2016) Outcomes of the Nymagee mineral system study—an improved understanding of the timing of events and prospectivity of the central Lachlan Orogen. *Quarterly Notes of the Geological Survey of New South Wales*, 147, 1–38.

Einaudi, M.T., Meinert, L.D. and Newberry, R.J. (1981) Skarn deposits. *Economic Geology*, 75th Anniversary Volume, 317–391.

Fergusson, C.L. (2017) Mid to late Palaeozoic shortening pulses in the Lachlan Orogen, southeastern Australia: a review. *Australian Journal of Earth Sciences*, 64, 1–39. https://www.tandfonline.com/doi/full/10.1080/08120099.2017.1273257.

Fitzherbert, J. A., Blevin, P. L. and McKinnon, A. M. (2017a) Turbidite-hosted intrusion-related mineralisation in the Cobar Basin: new insights from the south. Mines and Wines—Discoveries in the Tasmanides 2017. Extended Abstracts, AIG Bulletin 67. http://www.minesandwines.com.au/papers-2017/4_basins-and-more/.

Fitzherbert, J.A., Mawson, R., Mathieson, D., Simpson, A.J., Simpson, C.J. and Nelson, M.D. (2017b) Metamorphism in the Cobar Basin: current state of understanding and implications for mineralisation. *Quarterly Notes of the Geological Survey of New South Wales*, 148, 1–35.

Fitzherbert, J.A., Downes, P.M., Blevin, P.L., Norris, E., Huang, H., Matchan, E., Waltenberg, K., Wall, C. and Phillips, D. (2019) Refining the Cobar-type mineral system: new insights spawned from direct dating of mineralisation. Discoveries in the Tasmanides, AIG Bulletin 96.

Fortier, S.M. and Giletti, B.J. (1991) Volume self-diffusion of oxygen in biotite, muscovite, and phlogopite micas. *Geochimica et Cosmochimica Acta*, 55, 1319–1330.

Glen, R.A. (1982) Nature of late-Early to Middle Devonian tectonism in the Buckambool area, Cobar, New South Wales. *Journal of the Geological Society of Australia*, 29(1-2), 127–138.

Glen, R.A. (1987) Geology of the Wrightville 1:100,000 sheet 8034. Sydney: New South Wales Geological Survey.

Glen, R.A., Dallmeyer, R.D. and Black, L.P. (1992) Isotopic dating of basin inversion—the Palaeozoic Cobar Basin, Lachlan Orogen, Australia. *Tectonophysics*, 214, 249–268.

Glen, R.A. (1994) Geology of the Cobar 1:100 000 sheet 8035. Sydney: Geological Survey of New South Wales, 132 pp.

Glen, R.A., Clarke, A. and Spencer, R. (1996) Extrapolating the Cobar Basin model to the regional scale: Devonian basin-formation and inversion in western New South Wales. In: Cook, W.G., Ford, A.J.H., McDermott, J.J., Standish, P.N., Stegman, C.L. and Stegman, T.M. (Eds.) *The Cobar Mineral Field—1996*. Melbourne, Victoria, *Australasian Institute of Mining and Metallurgy*, Spectrum Series 3/96, 449 pp: Australasian Institute of Mining and Metallurgy, pp. 43–83.

Glen, R.A., Belousova, E. and Griffin, W.L. (2016) Different styles of modern and ancient non-collisional orogens and implications for crustal growth: a Gondwanaland perspective. *Canadian Journal of Earth Sciences*, 53, 1372–1415.

Gradstein, F., Ogg, J. and Hilgen, F. (2012) A Geologic Time Scale. *Newsletters on Stratigraphy*, 45(2), 171–188.

Graham, C.M., Sheppard, S.M.F. and Heaton, T.H.E. (1980) Experimental hydrogen isotope fractionation factors in the systems epidote-H_2O, zoisite-H_2O and AlO(OH)-H_2O. *Geochimica et Cosmochimica Acta*, 44, 353–364.

Graham, C.M., Harmon, R.S. and Sheppard, S.M.F. (1984) Experimental hydrogen isotope studies: Hydrogen isotope exchange between amphibole and water. *American Mineralogist*, 69, 128–138.

Graham, C.M., Viglino, J.A. and Harmon, R.S. (1987) Experimental study of hydrogen-isotope exchange between aluminous

chlorite and water and of hydrogen diffusion in chlorite. *American Mineralogist*, 72, 566–579.

Greenfield, J., Gilmore, P., Downes, P., Fitzherbert, J., Perks, C., Deyssing, L. and Gilligan, L. (2015) A review of metalliferous basins in New South Wales. Wines & Wines 2015. *AIG Bulletin*, 62, 93–110.

Hoefs, J. (Ed.). (2004) *Stable Isotope Geochemistry*. Germany: Springer.

Jones, S.L., Fitzherbert, J.A., Waltenberg, K. and Bodorkos, S. (2020) New SHRIMP U–Pb Ages from the Cobar Basin, New South Wales: Mineral Systems Projects, July 2018–June 2019. Record 2020/42. Geoscience Australia, Canberra.

Kositcin, N. (1999) *The Petrology and Geochemistry of the Avenall Basic Intrusive Complex, Southeastern New South Wales*. B.S.c Honours (Unpublished), 82pp + appendices. Canberra: Australian National University.

Lawrie, K.C. and Hinman, M.C. (1998) Cobar-style polymetallic Au-Cu–Ag–Pb–Zn deposits. *AGSO Journal of Australian Geology & Geophysics*, 17, 169–187.

Leeke, B.E., Woolley, A.R., Arps, C.E.S., Birch, W.D., Glibert, C.M., Grice, J.D., Hawthorn, F.C., Kato, A., Kisch, H.J., Krivovichev, V.G, Linthout, K., Laird, J., Mandarino, J. A., Maresch, W.V., Nickel, E.H., Rock, N.M.S., Schumacher, J.C., Smith, D,C,, Stephenson, N.C.N., Ungaretti, L., Whitake, E.J. W. and Youzhi, G. (1997) Nomenclature of amphiboles; Report of the Subcommittee on Amphiboles of the International Mineralogical Association, Commission on New Minerals and Mineral Names. *The Canadian Mineralogist*, 82(2), 1019–1037.

Lyons, P., Raymond, O.L. and Duggan, M.B. (Eds.). (2000) *Forbes Geological Sheet 1:250 000 S155-7 Explanatory Notes*. Canberra: Australian Geological Survey Organisation 230p.

Mathieson, D., Mawson, R., Simpson, A.J. and Talent, J.A. (2016) Late Silurian (Ludlow) and early Devonian Pragian conodonts from the Cobar Supergroup, western New South Wales, Australia. *Bulletin of Geosciences*, 91(3), 583–652.

Matthews, A., Goldsmith, J.R. and Clayton, R.N. (1983) Oxygen isotope fractionation between zoisite and water. *Geochimica et Cosmochimica Acta*, 47, 645–654.

McDougall, I. and Harrison, T.M. (1999) Geochronology and Thermochronology by the $^{40}Ar/^{39}Ar$ Method. 2nd edn. New York: Oxford University Press.

McKinnon, A.R. (2017) *Application of Normative Ore Mineralogy to Geological and Metallurgical Data Sets at the Hera au-Pb-Zn-Ag Mine, New South Wales, Australia, in Proceedings Tenth International Mining Geology Conference 2017*. Melbourne: The Australasian Institute of Mining and Metallurgy, pp. 63–74.

McKinnon, A.R. and Fitzherbert, J.A. (2017) New developments at the Hera Au-Pb-Zn-Ag mine, Nymagee. Mines and Wines—Discoveries in the Tasmanides 2017. Extended Abstracts. *AIG Bulletin*, 67, 1–17. http://www.minesandwines.com.au/papers-2017/4_basins-and-more/.

Meinert, L.D. (1992) Skarns and Skarn Deposits. *Geoscience Canada*, 19(4). Available at: https://journals.lib.unb.ca/index.php/GC/article/view/3773.

Mernagh, T.P. (2008) Question 3: what and where are the fluid reservoirs for a mineral system? In: van der Wielen, S. and Korsch, R. (Eds.) 3D Architecture and Predictive Mineral Analysis of the Central Lachlan Subprovince and Cobar Basin, New South Wales, Final Report for the Pmd*CRC T11 Project, Geoscience Australia, Canberra, 85–116.

Parrish, M.D., Collins, W.J., Hegarty, R.A., Gilmore, P.J. and Huang, H.-Q. (2018) Depositional age and providence of the Cobar supergroup. *Australian Journal of Earth Sciences*, 65, 1035–1048.

Perkins, C., Hinman, M.C. and Walshe, J.L. (1994) Timing of mineralization and deformation, peak au mine, Cobar, New South Wales. *Australian Journal of Earth Sciences*, 41, 509–522.

Raymond, O.L., Duggan, M.B., Lyons, P., Scott, M.M., Sherwin, L., Wallace, D.A., Krynen, J.P., Young, G.C., Wyborn, D., Glen, R. A., Percival, I.G. and Leys, M. (2000) *Forbes 1:250 000 Geological Sheet SI/55–07*, 2nd edition. Sydney, Geoscience Australia, Canberra: Geological Survey of New South Wales.

Raymond, O., Sherwin, L., Lyons, P. and Scott, M. (2000a) The Jemalong Trough: an extension of Silurian–Devonian rifting in the eastern Lachlan Fold Belt. *Geological Society of Australia, Abstracts*, 59, 409.

Rossetti, F. and Tecce, F. (2008) Composition and evolution of fluids during skarn development in the Monte Capanne thermal aureole, Elba Island, Central Italy. *Geofluids*, 8, 167–180.

Saccocia, P.J., Seewald, J.S. and Shanks, W.C. (2009) Oxygen and hydrogen isotope fractionation in serpentine–water and talc–water systems from 250 to 450°C, 50MPa. *Geochimica et Cosmochimica Acta*, 73, 6789–6804.

Seccombe, P.K., Jiang, Z. and Downes, P.M. (2017) Sulfur isotope and fluid inclusion geochemistry of metamorphic cu–au deposits, Central Cobar area, NSW, Australia. *Australian Journal of Earth Sciences*, 64, 537–556.

Spandler, C., Hammerli, J., Sha, P., Hilbert-Wolf, H., Hu, Y., Roberts, E. and Schmitz, M. (2016) MKED1: a new titanite standard for in situ analysis of Sm–Nd isotopes and U–Pb geochronology. *Chemical Geology*, 425, 110–126. https://doi.org/10.1016/j.chemgeo.2016.01.002.

Stacey, J.S. and Kramers, J.D. (1975) Approximation of terrestrial lead isotope evolution by a two-stage model. *Earth and Planetary Science Letters*, 26, 207–221. https://doi.org/10.1016/0012-821X(75)90088-6.

Stegman, C.L. (2001) Cobar deposits: still defying classification! *SEG. Newsletter*, 44(1), 15–26.

Stegman, C.L. (2007) 'Structural and geochemical controls on ore formation at the New Occidental gold deposit, Cobar, New South Wales, Australia', PhD thesis, University of Tasmania.

Sun, Y., Jiang, Z., Seccombe, P.K. and Feng, Y. (2000) New dating and a review of previous data for the development, inversion and mineralization in the Cobar Basin. In: McQueen, K.G. and Stegman, C.L. (Eds.) *Central West Symposium Cobar 2000, Extended Abstracts*, Queensland, Australia: CRCLEME, pp. 113–116.

Suppel, D.W. (1984) A study of mineral deposits in the Cobar Supergroup, Cobar region, New South Wales. MSc thesis, University of New South Wales, Sydney (unpubl.).

Suzuoki, T. and Epstein, S. (1976) Hydrogen isotope fractionation between OH-bearing minerals and water. *Geochimica et Cosmochimica Acta*, 40, 1229–1240.

Taylor, B.E. (1992) Degassing of H2O from rhyolite magma during eruption and shallow intrusion, and the isotopic composition of magmatic water in hydrothermal systems. *Geological Survey of Japan Report*, 279, 190–194.

Taylor, H.P. (1997) Oxygen and hydrogen isotope relationships in hydrothermal mineral deposits. In: Barnes, H.L. (Ed.) *Geochemistry of hydrothermal ore deposits* (third edition). New York, John Wiley, pp. 229–302.

Thomas, O.D. and Pogson, D.J. (2012) *Goulburn 12:250 000 Geological Sheet S1/55–12*, 2nd edition. Maitland, NSW: Explanatory Notes. Geological Survey of New South Wales.

van der Wielen, S.E. and Glen, R.A. (2008) MERNAGH T.P. 2008. Question 1: What are the geodynamic and pressure - temperature histories? In: van der Wielen, S. & Korsch, R. (Eds.) *3D architecture and predictive mineral analysis of the Central Lachlan Subprovince and Cobar Basin, New South Wales*, final report for the pmd*CRC T11 project. Geoscience Australia, Canberra, pp. 85–116.

Vennemann, T.W. and O'Neil, J.R. (1996) Hydrogen isotope exchange reactions between hydrous minerals and molecular hydrogen: I. a new approach for the determination of hydrogen isotope fractionation at moderate temperatures. *Geochimica et Cosmochimica Acta*, 60, 2437–2451.

Whitney, D.L. and Evans, B.W. (2010) Abbreviations for names of rock-forming minerals. *American Mineralogist*, 90, 185–187.

SUPPORTING INFORMATION

Additional supporting information may be found online in the Supporting Information section at the end of this article.

How to cite this article: Fitzherbert JA, McKinnon AR, Blevin PL, et al. The Hera orebody: A complex distal (Au–Zn–Pb–Ag–Cu) skarn in the Cobar Basin of central New South Wales, Australia. *Resource Geology*. 2021;71:296–319. https://doi.org/10.1111/rge.12262